

HIGH-RESOLUTION LOCAL EARTHQUAKE TOMOGRAPHY ACROSS THE
NEMAHA UPLIFT, NORTH-CENTRAL OKLAHOMA, USA

A Thesis

Presented to the Faculty of the Graduate School
of Cornell University

In Partial Fulfillment of the Requirements for the Degree of
Master of Science

by

Nathan Thomas Stevens

December 2018

© 2018 Nathan Thomas Stevens

ABSTRACT

Recent earthquakes in north central Oklahoma are primarily hosted on unmapped faults in the crystalline basement but are sparse in the largest regional structure, the Nemaha uplift. This absence is despite the presence of numerous high-rate salt water disposal wells near large faults of the uplift. This thesis presents compressional (V_p) and shear (V_s) tomographic velocity models across the uplift using a new catalog of 25,601 local earthquakes recorded by 131 local seismic stations operating between 2013 and 2017. Seismic velocities are consistent with expected basement geology outside the uplift; V_p and V_s values are diminished by upwards of 2.5% within the uplift. The decrease in seismic velocity is interpreted to represent increased fault density and increased fluid volume within the uplift, with an associated increase in basement permeability. An increase in permeability may inhibit the buildup of fluid pressure within the uplift, possibly contributing to local aseismicity.

BIOGRAPHICAL SKETCH

Nathan Stevens holds Bachelor and Master of Science degrees in Geosciences from The Pennsylvania State University where he researched ice-core physical properties, glacio-tectonics, and englacial hydrology. He has conducted two internships with the Chevron Exploration & Production Company where he implemented new microseismic processing workflows to monitor hydrofracture stages and developed a sequence stratigraphic framework for the Appalachian Basin in western Pennsylvania to aid well construction and geohazard prediction. His pursuit of a Master of Science degree at Cornell was motivated by a long-standing desire to gain experience as a seismologist and to one day apply these techniques to better understand glacier dynamics. Nathan is now a doctoral student at the University of Wisconsin – Madison researching glacier seismicity and basal sliding mechanics of alpine glaciers and Antarctic outlet glaciers as part of the ITGC (International Thwaites Glacier Collaboration) GHOST (Geophysical Habitat Of Subglacial Thwaites) project.

To my wife, Charlotte.

Without whom I may never have pursued my Personal Legend.

ACKNOWLEDGEMENTS

This research was supported by the National Science Foundation under CAREER Grant 1554846 and Rapid Grant 1663286. This work builds upon work presented in the thesis of by C. Lambert, who was funded in part by National Science Foundation grant DGE-1650441. I thank my committee members, Dr. Katie Keranen and Dr. Rowena Lohman for their guidance and support during this study. I thank Dr. Clifford Thurber for providing the TomoDD10 code and guidance in its implementation. Waveform data from 3 private stations were provided by Mr. Timothy Sickbert and collaborators at the Oklahoma State University. Operation of the XR and CU networks were aided by the efforts of C. Lambert, K. Crosbie, J.C. Garcia, D. Peterson, A. Hariharan, X. Wu, D. Quiros, L. McLeod, E. Norvel, and S. Zurkee (Cornell University students, alumni, & staff), as well as several volunteers from The Oklahoma State University, The University of Rochester, and The University of Oklahoma. Earthquake catalog development was aided by efforts of X. Wu. I sincerely thank the Oklahomans of Alfalfa, Garfield, Grant, Kay, Noble, Pawnee, and Woods Counties for hosting seismic stations of the XR and CU networks.

TABLE OF CONTENTS

Chapter 1: High Resolution Local Earthquake Tomography across the Nemaha Uplift	1
Introduction.....	1
Seismic Dataset: Initial Velocity Model and Earthquake Catalog.....	3
Methods: Double Difference Tomography	6
Methods: Sub-Catalog Development and Model Gridding for TomoDD Inversions.....	7
Methods: Model Parameterization & Resolution Testing.....	10
Results: Resolution Test Performance	16
Results: Inversion Performance with Observed Data	24
Results: Distribution of Seismicity.....	23
Results: Compressional Velocity Structure	25
Results: Shear Velocity Structure	28
Discussion: Vp/Vs Structure	32
Discussion: Faulting, Seismicity, and Basement Hydrology	32
Discussion: Compressional Velocity Structure, Seismicity, and Fault Distributions	33
Discussion: Shear Velocity Structure, Seismicity, and Fault Distributions	34
Discussion: Hypothesis of Compartmentalization in the Nemaha Uplift.....	35
Conclusions.....	35
References.....	37
Chapter 2: Supplementary Materials.....	41
Deployment Methods for the XR Network	41
Alternative Velocity Models and Earthquake Catalogs Inversion Results.....	46
2 Node by 2 Node Checkerboard Recovery Test Results	50
References.....	55
Appendix A: Earthquake Catalog Development Files.....	56
Appendix B: TomoDD Solution Control Files	69
Appendix C: Best Fit Inversion Directory & Initialization Instructions.....	73
Appendix D: Project Data Map	74

LIST OF FIGURES

Figure 1.1: Regional seismicity and mapped faulting in north central Oklahoma	2
Figure 1.2: Seismic stations and operator affiliations	4
Figure 1.3: Initial velocity model	6
Figure 1.4: Earthquake sub-catalog and gridding for TomoDD inversions.....	10
Figure 1.5: Parametric testing trade-off curve for differential damping	12
Figure 1.6: Checkerboard recovery test: 3x3 imposed velocity perturbation structure	15
Figure 1.7: 3x3 checkerboard test Vp recovery results 1.5-6 km BSL	19
Figure 1.8: 3x3 checkerboard test Vp recovery results 8-15 km BSL	20
Figure 1.9: 3x3 checkerboard test Vs recovery results 1.5-6 km BSL.....	21
Figure 1.10: 3x3 checkerboard test Vs recovery results 8-15 km BSL.....	22
Figure 1.11: Relocated earthquake sub-catalog	25
Figure 1.12: Recovered Vp structure and relocated earthquakes for 3-6 km BSL	27
Figure 1.13: Recovered Vp structure and relocated earthquakes for 8-12 km BSL	28
Figure 1.14: Recovered Vs structure and relocated earthquakes for 3-4.5 km BSL.....	30
Figure 1.15: Recovered Vs structure and relocated earthquakes for 6-8 km BSL.....	31
Figure 2.1: Double-walled vault interior	42
Figure 2.2: Double-walled vault pier hardware	42
Figure 2.3: XR network seismic station with single-walled vault	44
Figure 2.4: Alternative velocity model and input catalog inversion results.....	47
Figure 2.5: Dense earthquake sub-catalog	48
Figure 2.6: 2x2 checkerboard test Vp recovery results 1.5-6 km BSL	50
Figure 2.7: 2x2 checkerboard test Vp recovery results 8-15 km BSL	51
Figure 2.8: 2x2 checkerboard test Vs recovery results 1.5-6 km BSL.....	52
Figure 2.9: 2x2 checkerboard test Vs recovery results 8-15 km BSL.....	53

LIST OF TABLES

Table 2.1: Station sampling rates and operation dates	56
Table 2.2: dbdetect.PphaseBCEH.pf - P-wave arrival detection parameter file	60
Table 2.3: dbdetect.SphaseBCEH.pf – S-wave arrival detection parameter file.....	62
Table 2.4: ttgridnts.pf - Travel time grid parameter file.....	65
Table 2.5: dbgrassoc.test1.pf - Phase association & grid-search location parameter file....	67
Table 2.6: tomoDD.inp - Initial catalog relocation TomoDD control file.....	69
Table 2.7: tomoDD.inp - Best-fit parameterization TomoDD control file	71

LIST OF ABBREVIATIONS

CMG-3T	– Gralp Systems Broadband Seismometer
CU	– Network code for the Cornell University seismic array
CWB	– Central Waveform Buffer
DAS	– Data Acquisition System
DMC	– Data Management Center
DOY	– Day Of Year, or Julian Day
DWS	– Derivative Weighted Sum
GS	– IRIS network code for most USGS seismic stations
HypoDD	– Double Difference Hypocentral Relocation Method (Waldhauser & Ellsworth, 2000)
IRIS	– Incorporated Research Institutions for Seismology
KS	– Kansas, also the IRIS code for the KGS Seismic Network
MCR	– Mid-Continent Rift System
NFZ	– Nemaha Fault Zone
NQ	– IRIS network code for USGS NetQuake seismic stations
NX	– IRIS network code for the Nanometrics Experimental Array
OGS	– Oklahoma State Geological Survey
OK	– Oklahoma, also the IRIS code for the OGS Seismic Network
OK-KS	– The north-central Oklahoma and south-central Kansas region
OSU	– Oklahoma State University
sps	– samples per second
SR	– Sampling Rate
SU	– Network code for the OSU seismic network
SWD	– Salt Water Disposal
TomodD	– Double Difference Tomography Method (Zhang & Thurber, 2003, 2006)
USGS	– United States Geological Survey
XR	– IRIS network code for the Oklahoma Gap Seismic Experiment
ZD	– IRIS Network code for select USGS seismic stations

LIST OF SYMBOLS

- d** – Observed data vector
- G** – Design matrix of partial derivatives
- Gm** – Matrix multiplication of **G** and **m**, equivalent to modeled data
- m** – Model vector, containing parameter estimates
- m_o** – Initial model vector, containing starting parameter estimates
- M_w – Moment magnitude
- pDWS – Compressional phase DWS
- sDWS – Shear phase DWS
- V_p – Compressional (P-wave) Velocity
- V_{p,o} – Initial Compressional Velocity
- V_p/V_s – Ratio of compressional and shear velocities
- V_s – Shear (S-wave) Velocity
- V_{s,o} – Initial Shear Velocity
- $\| \underline{*} \|$ – The L-2 norm of the input vector $\underline{*}$

CHAPTER 1

HIGH-RESOLUTION LOCAL EARTHQUAKE TOMOGRAPHY ACROSS THE NEMAHA UPLIFT

Introduction

The massive increase in the rate of seismicity across the United States mid-continent over the past decade has been strongly linked to salt water disposal (SWD) into deep sedimentary formations and fractured crystalline basement (e.g. Ellsworth, 2013; Weingarten et al., 2015). Seismicity has increased in north-central Oklahoma and southern Kansas (OK-KS) (Keranen et al., 2013; Keranen et al., 2014; Yeck et al., 2016; Hincks et al., 2018), and in Arkansas (e.g., Horton, 2012), Ohio (e.g., Kim, 2013), and Texas (e.g., Frohlich et al., 2011). In OK-KS, seismicity is largely hosted within the crystalline basement on faults not expressed in the sedimentary cover (McNamara et al., 2015; Marsh & Holland, 2016; Lambert, 2017; Schoenball & Ellsworth, 2017b, 2017a). The primary fault-bounded basement structures of the region exhibit relatively little seismic activity (Figure 1.1, after Lambert, 2017), most notably the Nemaha uplift in OK-KS, regions west of the Nemaha Fault Zone (NFZ) in central Oklahoma, and faults in Woods and Alfalfa counties.

Estimates of maximum horizontal stresses in the region suggest that mapped faults of the NFZ are poorly oriented for failure, and that faults in Woods and Alfalfa counties are optimally to sub-optimally aligned for failure (e.g., Alt & Zoback, 2017). Stress field alignment does not fully explain low rates of seismicity along well-aligned portions of these faults. Recent regional body-wave tomography studies (Chen, 2016; Pei et al., 2018) have limited station coverage across the Nemaha uplift and do not recover velocity structure in the seismogenic crust on the scale of individual fault-bounded blocks (10-20 km length scales,, Marsh & Holland, 2016). Crustal-phase

anisotropy does indicate fast-axis alignment along Nemaha uplift, likely suggesting a preferred orientation of faults (Pei et al., 2018).

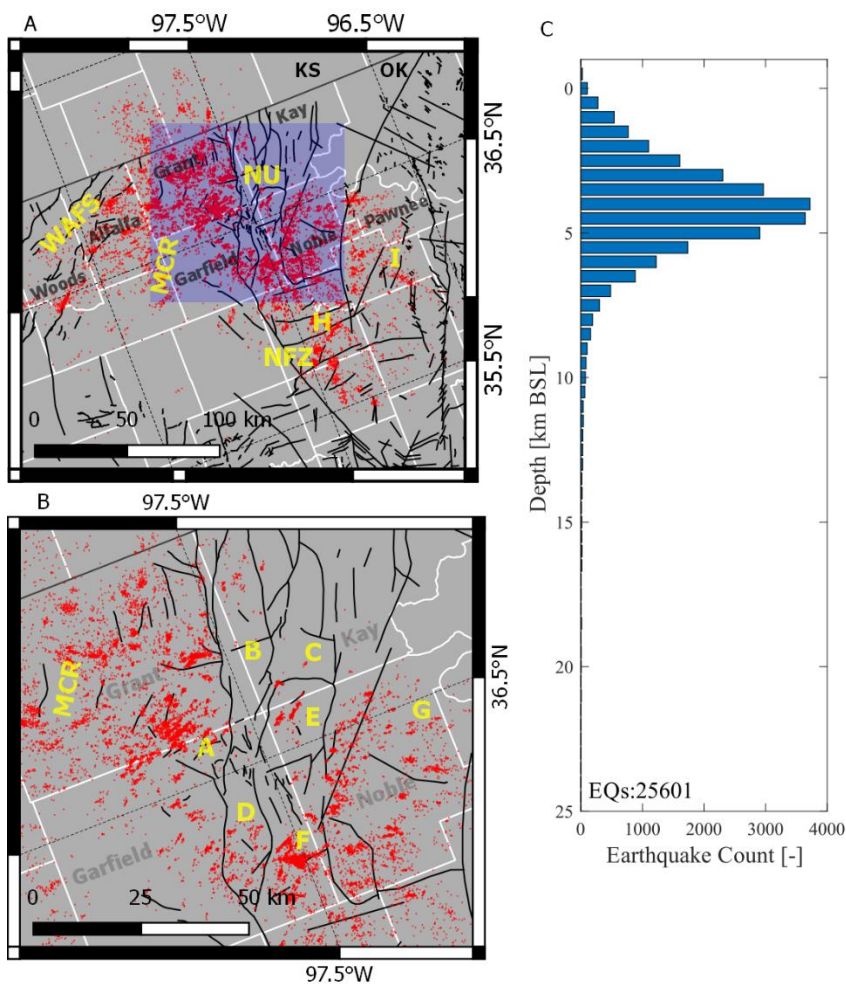


Figure 1.1: Map of initial, relocated earthquake catalog locations developed in this thesis and by Lambert (2017; red dots) for seismicity in the OK-KS region between 2013 and 2017. Mapped faults in Oklahoma are shown as black traces (after Marsh & Holland, 2016; note: fault data are unavailable for Kansas). (A) Major fault-bounded structures and regions of interest in this study are labeled. WAFS: Woods-Alfalfa County Fault System, NU: Nemaha Uplift, NFZ: Nemaha Fault Zone, and regions of interest labeled H, & I. (B) Subset map of the Nemaha uplift (blue box in A) with major blocks of the uplift labeled A, B, C, D, E, F, & G discussed in this study. (C) Depth distribution of catalog earthquakes; 500 m depth bins. County boundaries are shown in white and select counties are labeled. This, and every subsequent figure is rotated 21° west of north to align with the trace of the Nemaha uplift. Depths are reported in kilometers below sea level (km BSL)

New data from dense seismic arrays that spanned the Nemaha uplift between 2015 and 2017, and supplementary data from deployments in OK-KS between 2013 and 2017, were used in the high-resolution body-wave tomography for the uppermost crust in north-central Oklahoma, presented here. Tomographic imaging yielded 3-D compressional (V_p) and shear (V_s) velocity structure, resolving features on the scale of blocks of the NFZ (10-20 km, Figure 1.1.B). Velocities exhibit strong spatial correlation with mapped fault structures, with recovered values consistent with basement seismic velocities. V_p and V_s values within the uplift are lower than those on either side. The spatial correlation between known structures, reduced seismic velocities, and the relative absence of seismicity within the Nemaha uplift suggest increased hydrologic permeability within the uplift, which may reduce fluid pressure and induced seismicity.

Seismic Dataset: Initial Velocity Model and Earthquake Catalog

The Oklahoma Gap Seismic Experiment (IRIS Network XR) (Figure 1.2) included 41 CMG-3T broadband seismometers and 4 EpiSensor accelerometers deployed from February 2016 to June 2017 (Figure 1.2; data acquisition summary in Table 2.1; Appendix A). The full network was installed by late March 2016, and 38 of these stations remained in-place for the duration of the deployment. Seven stations comprised a “flex” array used to supplement aftershock deployments following the Mw 5.1 Fairview (February 2016) and Mw 5.8 Pawnee (September 2016) earthquakes, and to extend the breadth of the network across the seismically active portion of the Mid-Continent Rift (MCR) in early 2017 (golden triangles in Figure 1.2). Three-component data from these instruments were recorded at 200 samples per second (sps), with periods of operation at 100 sps and 250 sps depending on

operational needs (see Table 2.1; Appendix A). Images and details on station deployment methods are documented in Chapter 2.

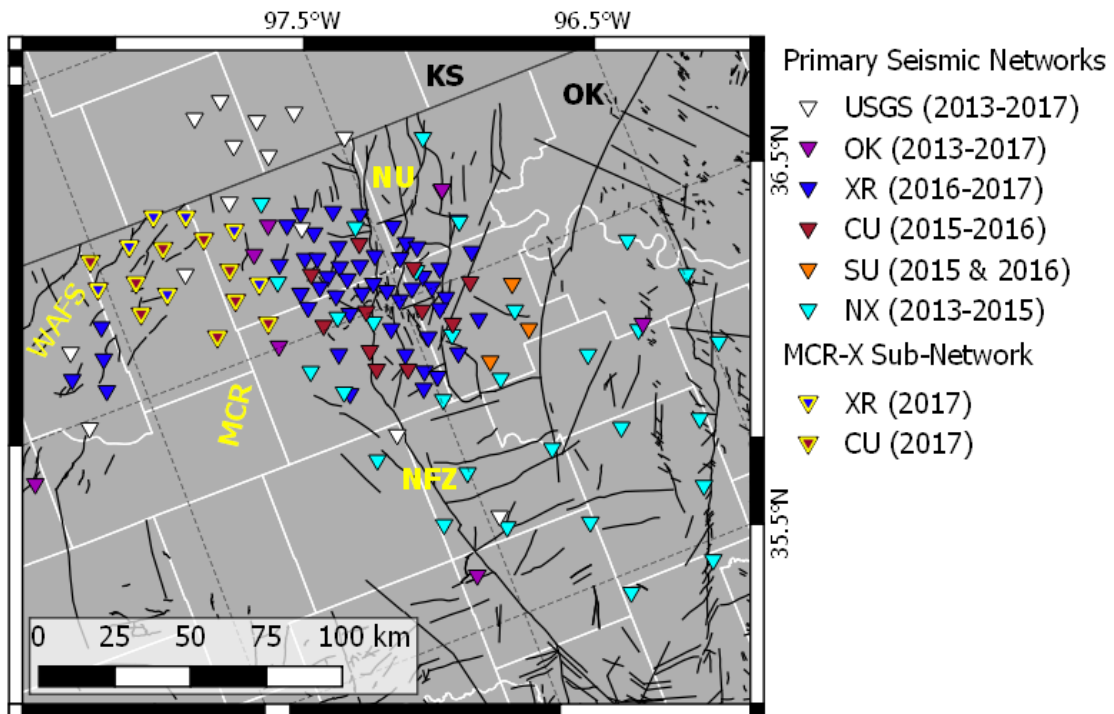


Figure 1.2: Seismic station locations (triangles) and map-view model grid nodes implemented in this study. Stations are colored according to network grouping. Faults, feature labels, and political boundaries match Figure 1.1.

Data from the XR network were supplemented with 10 private instruments from the Cornell Seismic Network (network code CU) initially deployed across the NFZ in 2015 (Lambert, 2017) and later re-deployed to extend the network to the west. Select waveform data were provided from a private network by collaborators at the Oklahoma State University (network code SU). Further waveform data from deployments spanning 2013 to 2017 were acquired from the Oklahoma Geological Survey Network (network code OK at the Incorporated Research Institutions for Seismology Data Management Center IRIS DMC) and from USGS networks GS, ZD, and NQ (via the USGS Central Waveform Buffer). These assembled data represent 131 unique station locations operational between 2013 and 2017 across the OK-KS

region. The composite array has an effective station spacing ranging from 5 km in its core to 25 km at the periphery (Figure 1.2).

Multiple velocity models exist from other studies of earthquake catalog and earthquake tomography in Oklahoma (Darold et al., 2015; Chen, 2016; Lambert, 2017; Schoenball & Ellsworth, 2017b; Pei et al., 2018; Zhu, 2018). These studies used initial velocity models based on refraction study results (Tryggvason & Qualls, 1967; Mitchell & Landisman, 1970). With the exception of Lambert (2017), these studies derive V_s structure under the assumption of uniform V_p/V_s values of either 1.73 (Christensen, 1996; Darold et al., 2015) or 1.78 (Schoenball & Ellsworth, 2017b). However, laboratory studies indicate that V_p/V_s values for the upper crust across OK-KS may be as low as 1.67-1.70 (Katz et al., 2001; Katz & Reches, 2004). Similar values are recovered by regional tomography (Chen, 2016).

In this study, the velocity model from Lambert (2017) was used for initial earthquake catalog development. This initial catalog was relocated using the velocity model from Darold et al. (2015) and their model was used as the initial velocity model for tomographic inversions in this study (Figure 1.3). Event phase arrivals were detected and associated into an initial earthquake catalog using a short-term-average / long-term-average detection trigger (e.g., Withers et al., 1998) and a grid-search association and location routine in Antelope (parameter files in Appendix A, Tables 2.2-2.5). The initial catalog consisted of 25,394 candidate earthquakes, defined as association of ≥ 8 phases that could be located by the grid-search algorithm. This initial catalog contains 393,217 P-arrivals and 299,220 S-arrivals.

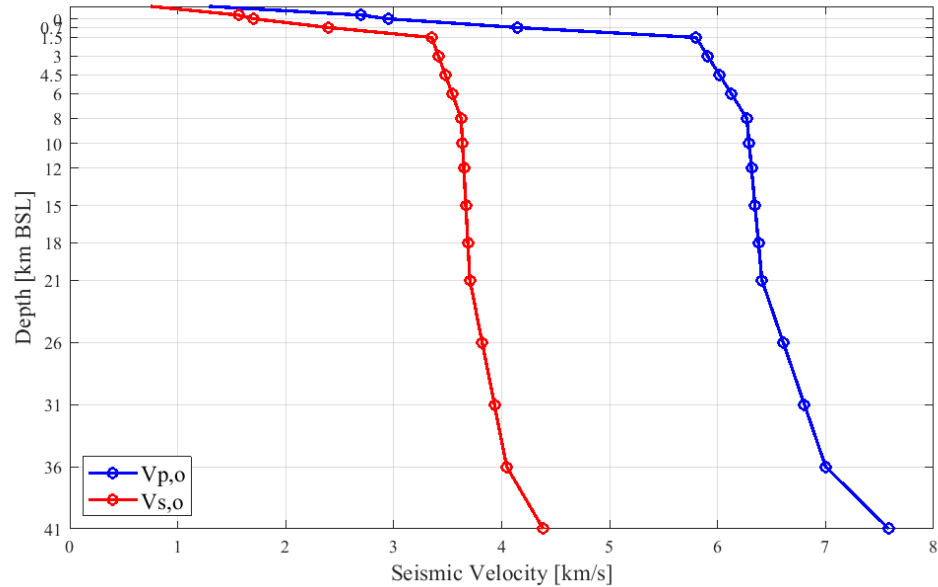


Figure 1.3: Initial compressional ($V_{p,o}$; blue) and shear ($V_{s,o}$; red) vertical velocity profiles. Model depth grid nodes are labeled on the vertical axis.

Methods: Double Difference Tomography

This study implements the double-difference tomography (TomoDD) method of Zhang & Thurber (2003, 2006) to simultaneously invert for compressional velocity structure (V_p), shear velocity structure (V_s), and hypocentral locations. This method builds upon the double-difference hypocentral relocation method (HypoDD) of Waldhauser & Ellsworth (2000), incorporating absolute travel time data to allow for absolute event location and tomographic imaging, and inversion of differential travel times to refine source-region velocity structure while also conducting relative event relocation. Differential travel times are calculated for event pairs within a defined radius and station-event pairs within a defined distance (see Waldhauser & Ellsworth, 2000).

TomoDD implements an iterative, damped least squares approach to solving both the earthquake location and tomography problems. Early iterations use absolute phase travel time data to estimate absolute event locations and velocity structure, and

later iterations use differential travel time data to refine relative event locations within sub-regions and the velocity structure of these source regions. A hierarchical weighting scheme is implemented here to favor absolute travel time data in early iterations and differential travel time data in later iterations (after Zhang & Thurber, 2003, 2006).

The inversion for velocity structure in TomoDD converges faster than the hypocentral relocation inversion by a factor of ~ 2 (Zhang & Thurber, 2006), thus event relocation inversions (relocation-only-inversions) are conducted in each iteration, while tomography inversions are conducted every other iteration, alongside relocation inversions (coupled-inversions). This approach encourages more-uniform convergence of inversion components. This alternating inversion scheme is implemented in this study, the full control file of which is documented in Table 2.7; Appendix A.

The V_p/V_s ratio of rocks can provide useful diagnostic information about the composition and mechanical properties of the crust (e.g., Moos & Zoback, 1983), but is not as robustly recovered by TomoDD (e.g., Watkins et al., 2018). Inversion results for V_p/V_s structure data are provided in Appendix C, using direct division of V_p and V_s rather than a direct inversion for V_p/V_s structure as conducted by other inversion methods (e.g., simul2000). Accurate V_p/V_s structure relies on equivalent recovery of V_p and V_s structure, both in the spatial distribution and magnitude of velocity values (Zhang & Thurber, 2006, 2007).

Methods: Sub-Catalog Development and Model Gridding for TomoDD Inversions

The TomoDD method requires numerous, but distributed, earthquakes to provide sufficiently dense intersecting ray-paths to resolve velocity anomalies, with sufficiently few redundant ray-paths to avoid inversion instability. Sufficiently dense

event spacing increases the number of differential travel time observations that inform event location refinement and source-region velocity structure (Zhang & Thurber, 2003, 2006, 2007; Thurber et al., 2007; Zhang et al., 2009). V_p and V_s structure recovery is more robust if similar P and S phase counts are used (Zhang & Thurber, 2007).

The initial earthquake catalog required refinement to limit the number and density of events and to balance the phase counts between P and S travel time data. Events with fewer than 12 observations were filtered out, and the remaining events were relocated using a single relocation-only-inversion of TomoDD to refine initial locations and to remove earthquakes with anomalously large data residuals (> 1 second). This inversion included both absolute travel time data and differential travel time data for event pairs within 25 km of one another and for station-event pairs within 200 km of one another (roughly 75% of the long-axis of the array, Figure 1.2). Relocated events were then filtered to only include those events with P:S data ratios less than or equal to 2:1, to encourage balanced velocity structure recovery for both V_p and V_s structure (Zhang & Thurber, 2007). The remaining earthquakes were spatially declustered to keep only the most data-rich earthquakes. Events were sorted by descending phase count and earthquakes were progressively pruned by centering an oblate spheroid on a given event and keeping the single most phase-rich event within the volume of the spheroid. The sub-catalog presented in Figure 1.4 had spheroids defined by a vertical radius of 0.5 km and a lateral radius of 2.5km, following the methods of Thurber et al. (2007) and Dunn et al. (2013). These lateral and vertical distances were selected as a quarter of the velocity model layer thicknesses at seismogenic depths and half the minimum station spacing. Additionally, events shallower than 1 km BSL and deeper than 20 km BSL were removed (compare Figure 1.1.B and 1.4.B).

The resultant sub-catalog of 3,103 events (12.2 % of the initial earthquake catalog) consists of 52,587 P-travel time data and 36,710 S-travel time data (13.4% and 12.3% of the initial phase counts, respectively). Differential travel times were calculated for event pairs within 25 km of one another and station-event pairs within 200 km of one another, resulting in 100,871 event pairs with 1,093,435 P-differential travel times and 620,054 S-differential travel time data with an average of 16 phase-pairs per event pair. An alternative sub-catalog, using earthquakes declustered with a vertical radius of 0.5 km and a lateral radius of 1.25 km spacing was assessed and produced similar inversion results. The event distribution of this sub-catalog and select examples from its inversion are presented in Chapter 2 (Figures 2.4 & 2.5).

The tomography model grid spacing was selected to match minimum station spacing (5 km node spacing) across the XR array, tapering to 10 km node spacing for 5 nodes on each edge of the model (crosses, Figure 1.4). Padding nodes at 20 km spacing were added to prevent edge effects. Vertical node spacing was set based on expected depth resolution with a 2 km spacing across seismogenic depths and increasing node spacing below.

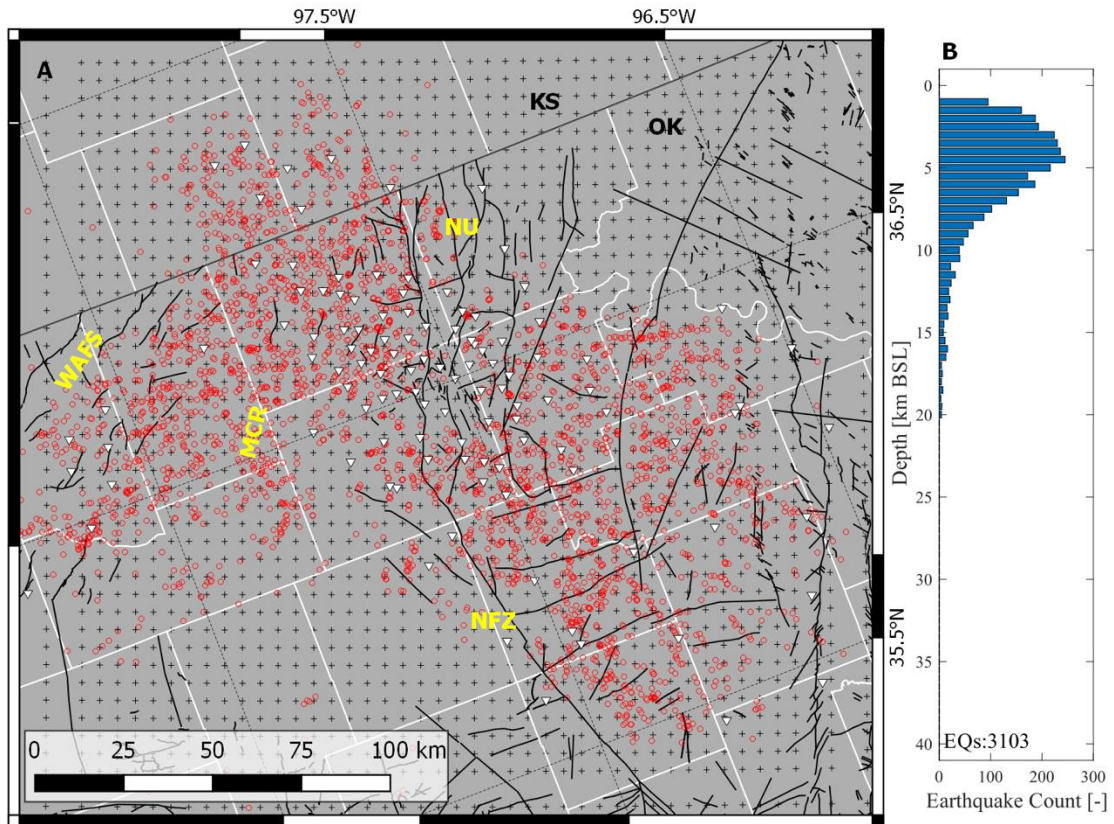


Figure 1.4: Input earthquake sub-catalog (A) epicentral locations (red circles), station locations (triangles), and model node locations (black crosses) used to conduct tomographic inversions in this study. (B) Depth distribution of sub-catalog earthquakes. Faults, features, and political boundaries match Figure 1.1.

Methods: Model Parameterization & Resolution Testing

We sought an optimized inversion parameterization through variation of damping and smoothing parameters across 101 model realizations. Within a given model realization, damping terms were held constant for successive iterations of relocation-only-inversions and coupled-inversions (e.g., Dunn et al., 2013; Watkins et al., 2018). Further, we investigated differential damping schemes, where damping terms were independently varied across a 2-D parameter space. Differential damping parameterization results are shown as a trade-off curve (Figure 1.5), where damping

values range from 75 to 400. The best-fit parameterization of an inversion is considered the balancing point between the minimization of data residuals and the minimization of model complexity (e.g., Eberhart-phillips, 1986). In the case of the trade-off curve shown in Figure 1.5, this best-fit parameterization corresponds to the model realization for which the distance from the origin (i.e., no residuals and no model complexity) is minimized. Relocation-only-inversion damping shows the greatest influence on parametric distance minimization while coupled-inversion damping exerts secondary control. Parametric search results in Figure 1.5 show an optimal trade-off in the L-2 norm of model complexity and data residuals for a damping scheme for a relocation-only-inversion damping value of 75 and coupled-inversion damping value of 200 (Figure 1.5, red dot). Coupled-inversion damping values ranging from 150-250 paired with relocation-only-inversion damping values of 75 produced similar, but slightly larger distance values from the origin. Previous studies use uniform damping values for both types of inversions (e.g. Zhang et al., 2009; Dunn et al., 2013; Watkins et al., 2018). Comparison of uniform parameterization (model realizations connected by the black line in Figure 1.5) to differential damping parameterization (blue & red dots, Figure 1.5) shows improved minimization of the parametric distance for 43 of the 101 model realizations.

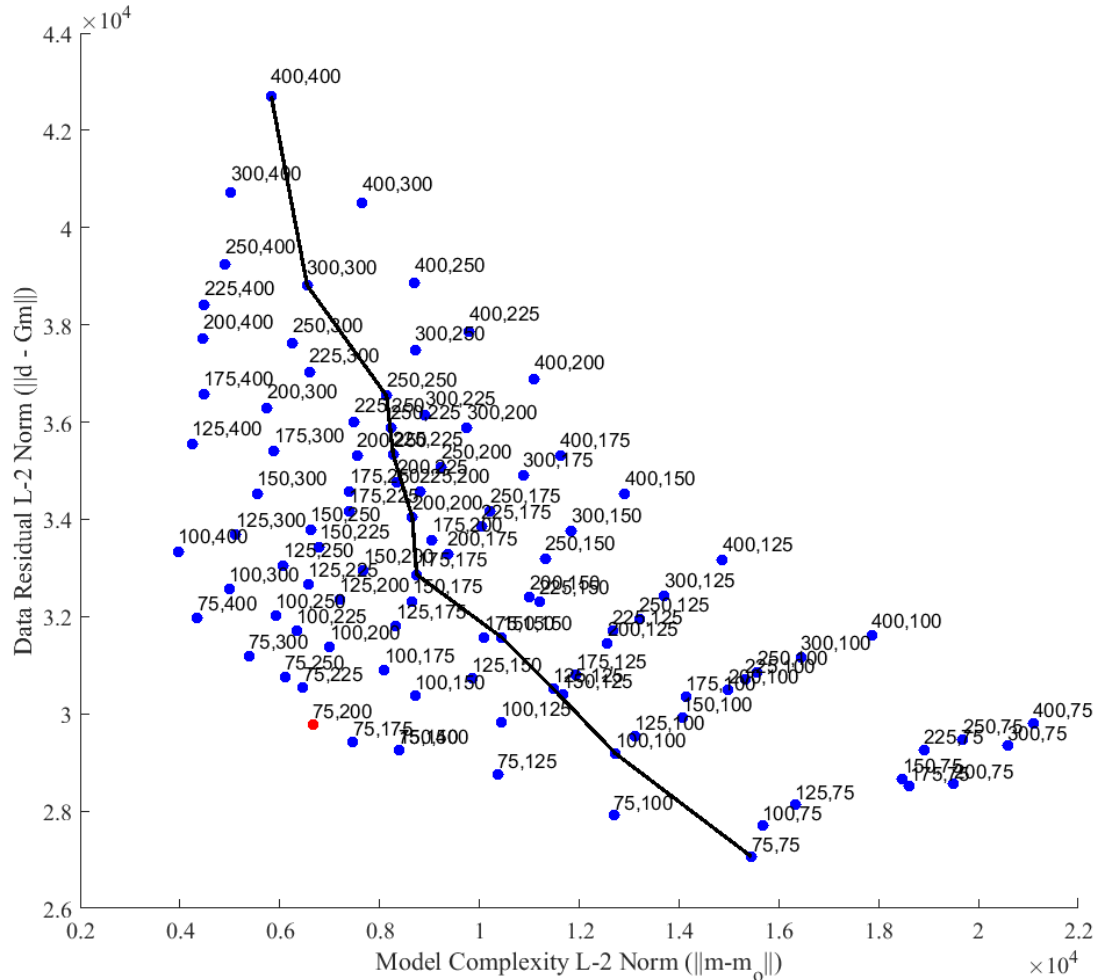


Figure 1.5: Differential damping results, comparing the L-2 norms of model complexity ($\|\mathbf{m}-\mathbf{m}_0\|$) and data misfit ($\|\mathbf{d}-\mathbf{G}\mathbf{m}\|$), where \mathbf{d} represents the data vector, \mathbf{G} the design matrix, and \mathbf{m} the model vector, with \mathbf{m}_0 representing the initial model vector. Points are labeled with the relocation-only-damping value followed by the coupled-inversion-damping value. The parametric curve associated with equal relocation-only-inversion-damping and coupled-inversion-damping values is shown in black. The “best-fit” parameterization is shown in red.

We examined a range of smoothing values for both vertical and lateral smoothing, ranging from 1-50, but this variation exerted only minor control on optimization of the trade-off curve. Larger smoothing values suppress large velocity structure perturbations in the shallowest model nodes (< 3 km BSL) where ray-paths are almost exclusively up-going. Smoothing terms from 10-20 sufficiently suppress

these artifacts without over smoothing other features. We use vertical smoothing values of 10 and lateral smoothing values of 15, consistent with the best-fit parameterization of Dunn et al. (2013).

The TomoDD method outputs ray-path density within a given inversion iteration using a derivative weighted sum (DWS) at each model node. Previous studies demonstrate that DWS thresholds, combined with checkerboard recovery testing, provides a suitable proxy for the formal resolution matrix when examined after inversion (e.g., Toomey & Foulger, 1989; Zhang & Thurber, 2007). This approach uses contours of equal DWS to bound regions of recovered velocity structure from the synthetic checkerboard test. DWS values are calculated for both V_p (pDWS) and V_s (sDWS) during ray-tracing in each coupled-inversion. Therefore, recovered V_p and V_s structure resolution should be assessed according to the appropriate phase type. DWS threshold values provide a criterion for model resolution when examining inversion results that use observed data. Depending on the geometry of events and seismometers, any number of checkerboard recovery tests can be devised to assess model resolution.

Within a TomoDD simulation DWS values are also used for solution control during coupled-inversion iterations to prevent velocity perturbation at nodes that are sparsely informed (i.e., very few ray paths). If a minimum phase-specific DWS is not achieved within a given iteration for a given node, then it is not perturbed, which helps suppress large velocity anomalies at the edges of recovered velocity structure. Results presented here used a minimum DWS value of 0.2, although values ranging from 0.01-10 were examined. This minimum DWS value is not the same as the DWS threshold used in post-inversion resolution analysis described above.

Inversion results recovered low amplitude velocity perturbations ($< 3\%$ divergence from the initial velocity model), motivating use of $\pm 3\%$ anomalies in

synthetic recovery tests used here. To investigate resolution at several depth nodes simultaneously, a 3-dimensional checkerboard recovery test like that of Dunn et al. (2013) is implemented here. The checkerboard velocity model consists of laterally extensive checkerboard-patterned velocity perturbations placed at the approximate depths of the sediment-basement interface (3 km; Higley et al., 2014, and references therein), another near the depth of peak seismicity (6 km; Lambert, 2017; Schoenball & Ellsworth, 2017b), and two more at boundaries near 10 km and 15 km identified in early inversion results. The imposed layer perturbations and their vertical distribution are shown in Figure 1.6.

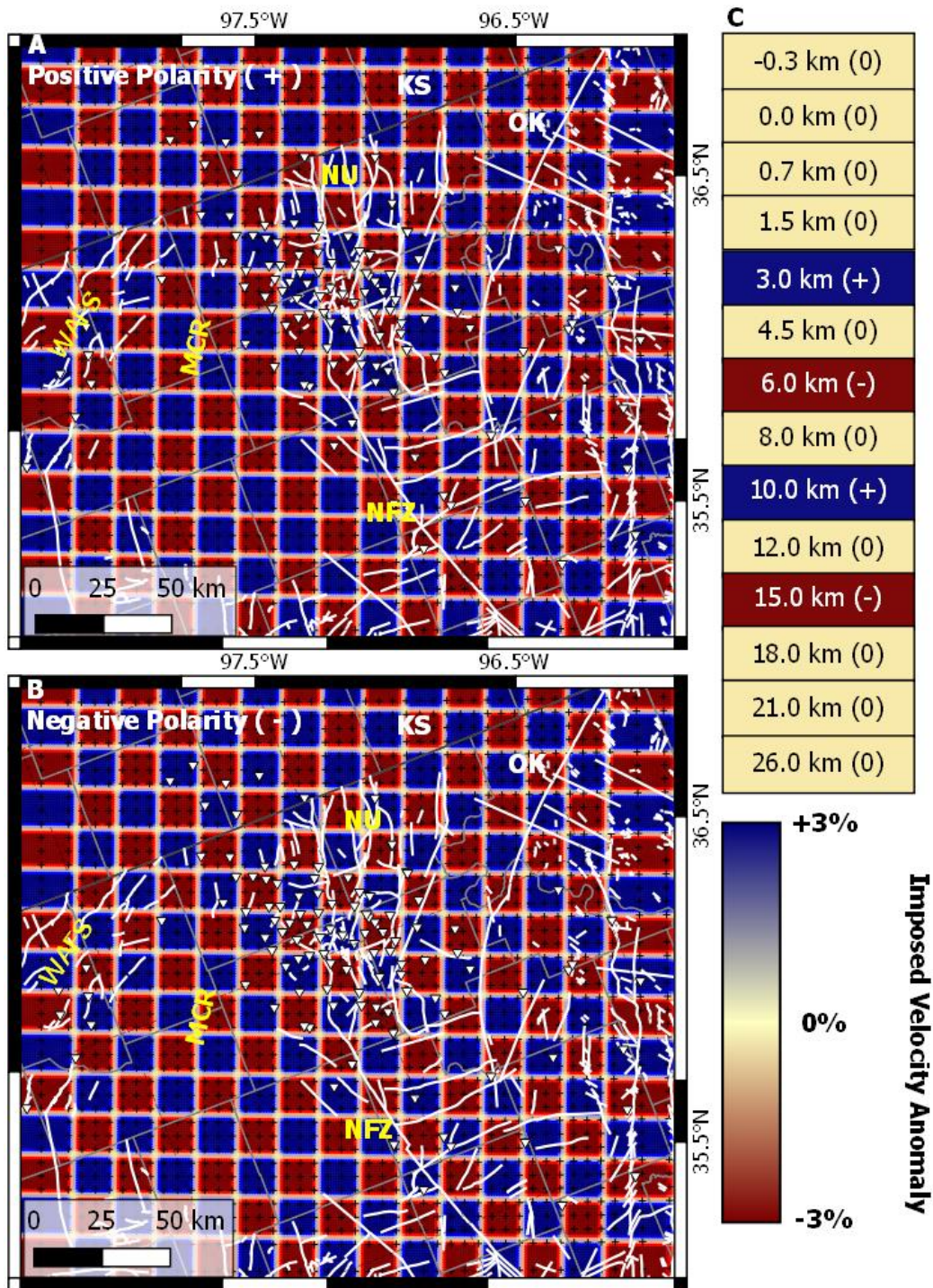


Figure 1.6: Imposed checkerboard anomalies implemented in synthetic recovery tests. Patterns shown here consist of 3-node by 3-node perturbations with (A) positive polarity, and (B) negative polarity. (C) Vertical distribution of these layers with (+) representing positive polarity, (-) representing negative polarity, and (0) representing no synthetic perturbation. Faults, features, and political boundaries match Figure 1.1. Station locations (white triangles) and grid points (black crosses) are shown.

Synthetic absolute travel time data were generated using the pseudo-ray bending routine in TomoDD for phase-event-station combinations present in the sub-catalog (Um & Thurber, 1987; Zhang & Thurber, 2003, 2006). All absolute travel time data were modified with a white noise term to simulate picking errors, with 0.02 sec maximum for P-phase data and 0.05 sec maximum for S-phase data, similar to values implemented by Dunn et al. (2013). Synthetic differential travel times were generated from the synthetic absolute travel times using the same spatial restrictions as the real sub-catalog data. Velocity structures were then recovered using the synthetic data and the inversion parameterization established through parametric testing (Table 2.7, Appendix B). Results were compared against the known synthetic velocity model to assess the resolving power of the inversion.

Results: Checkerboard Recovery Test Performance

The checkerboard inversion results, using synthetic data, for V_p and V_s structure are subdivided into “shallow” (1.5-6 km, Figures 1.7 and 1.8, respectively) and “deep” (8-15 km, Figure 1.9 and 1.10, respectively) depth slices. DWS thresholds are contoured at values of 50 and 150 for pDWS and sDWS, where noticeable changes in the quality of recovered velocity structure compared to the known synthetic velocity model were observed.

For shallow depths, values of pDWS > 50, the sign of imposed anomalies and some structure is recovered (Figures 1.7 & 1.9). For sDWS > 50, sign is recovered, but the shape of anomalies is only partially recovered (Figures 1.8 and 1.10). At pDWS > 150, both structure and amplitude of anomalies are recovered with over 80% recovery of V_p anomalies at seismogenic depths (Figure 1.7). For sDWS > 150, velocity structure is recovered but imposed anomaly amplitudes at seismogenic depths rarely

exceed 50% recovery (Figure 1.8). Recovered velocity structure quality systematically diminishes below 8 km BSL (Figures 1.9.A and 1.10.A). The regions with $pDWS > 150$ correspond to recovered V_p sign and structure, but limited amplitude recovery. Regions where $sDWS > 150$ only anomaly sign is recovered. Detailed analysis of checkerboard anomaly recovery between 1.5-15 km BSL are discussed below to establish DWS resolution thresholds for velocity structure recovered using synthetic data based upon the observed data. In turn, this establishes resolution criteria for the interpretation of velocity structure recovered by inversion of the observed data.

The 1.5 km checkerboard depth slice (Figures 1.7.A and 1.8.A), which included no input checkerboard structure, includes output checkerboard patterns in both V_p and V_s . Perturbations are up to $\pm 1.0\%$ within the $DWS > 150$ contour. This indicates vertical smearing from the imposed checkerboard pattern at the 3.0 km depth node (see layering in Figure 1.6.C). The 3.0 km checkerboard depth slice (Figures 1.7.B and 1.8.B), with an initial checkerboard structure, shows recovery of the imposed V_p anomalies within the $pDWS > 150$ contour, across a ~ 120 km by ~ 80 km region, where velocity perturbations of 2.2% (of the input 3%) are recovered (V_p range: 5.78–6.02 km/s). V_s structure within the $sDWS > 150$ contour, a ~ 60 km by ~ 40 km region, recovers perturbations up to 2.1% of the input 3% (V_s range: 3.34–3.46 km/s).

The 4.5 km checkerboard test depth slice (Figures 1.7.C and 1.8.C), with no input checkerboard structure, shows recovery of checkerboard structure and sign convention similar to the 3.0 km depth slice, indicating vertical smearing from the 3.0 km BSL imposed anomaly. Perturbations are up to 1.5% (V_p range: 5.93–6.06 km/s) across a ~ 140 km by ~ 100 km region (Figure 1.7.C). Bleeding in V_s structure occurs across a ~ 80 km by ~ 50 km region where $sDWS > 150$, recovering checkerboard perturbations up to 1.4% (V_s range: 3.43–3.51 km/s; Figure 1.8.C). Mean

perturbations of V_p and V_s remain below an 0.5% perturbation from initial layer velocities. The 6.0 km checkerboard test results (Figures 1.7.D and 1.8.D), with input checkerboard structure, at $pDWS > 150$ recover 2.7% anomalies (of the input 3%) across much of this region and 3.0% anomalies in select places (V_p range 5.88–6.32 km/s, V_{po} : 6.13 km/s; Figure 1.7.D). V_s results show a distinct checkerboard structure for $sDWS > 150$, recovering perturbations of up to 1.7% (V_s range: 3.48 km/s–3.60 km/s, V_{so} : 3.54 km/s).

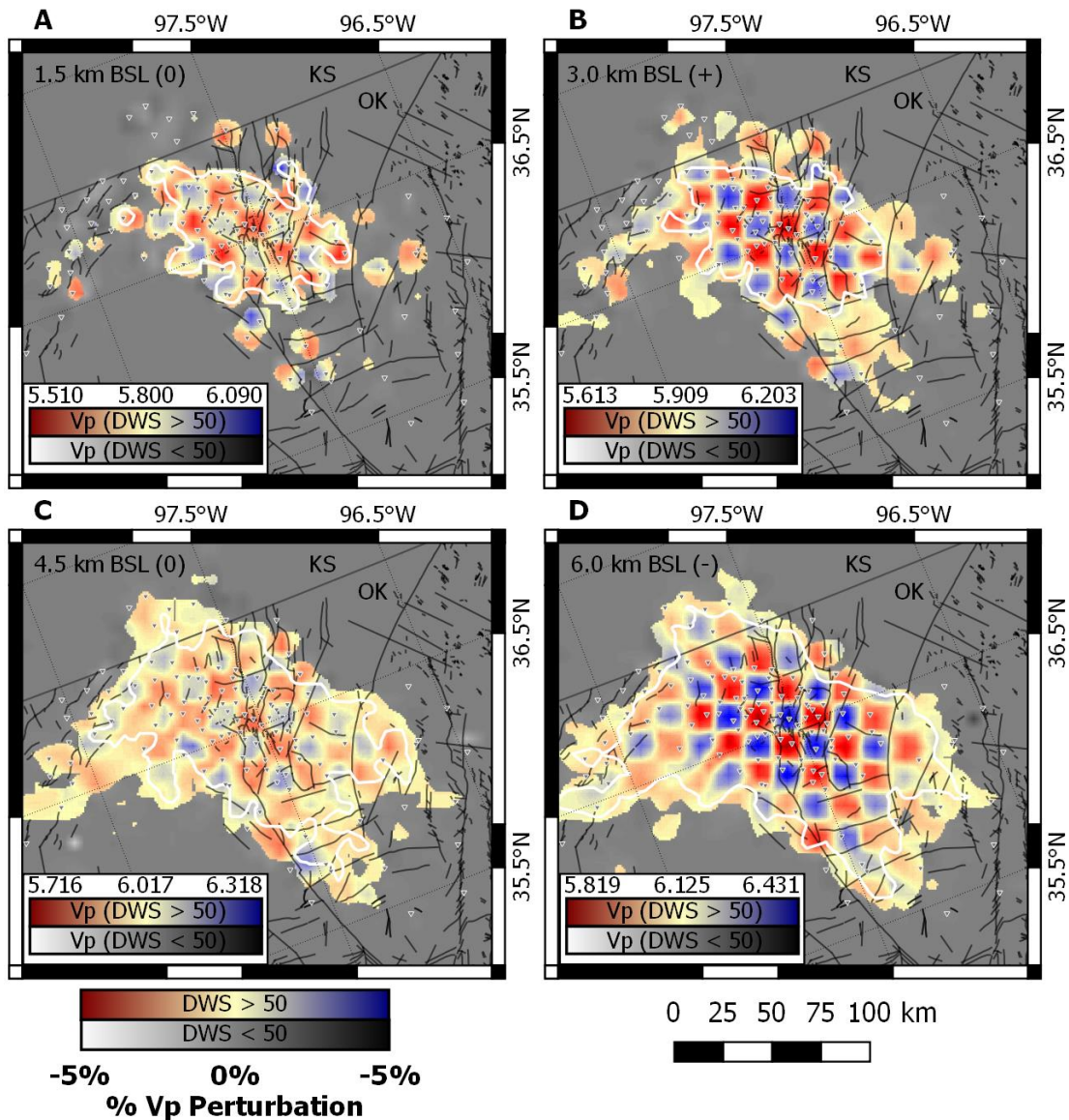


Figure 1.7: Shallow checkerboard recovery test results for V_p structure at the (A) 1.5 km, (B) 3.0 km, (C) 4.5 km, and (D) 6.0 km depth slices. The sign of imposed anomalies is shown in each figure corresponding to Figure 1.6.C. The transition from grayscale to colored results represents the $DWS = 50$ threshold, while the $DWS = 150$ threshold is represented by the white contour. Faults and political boundaries match Figure 1.1. Note that the color scale has been expanded from 3% to 5% to accommodate overestimation in recovered values. Velocities in km/s.

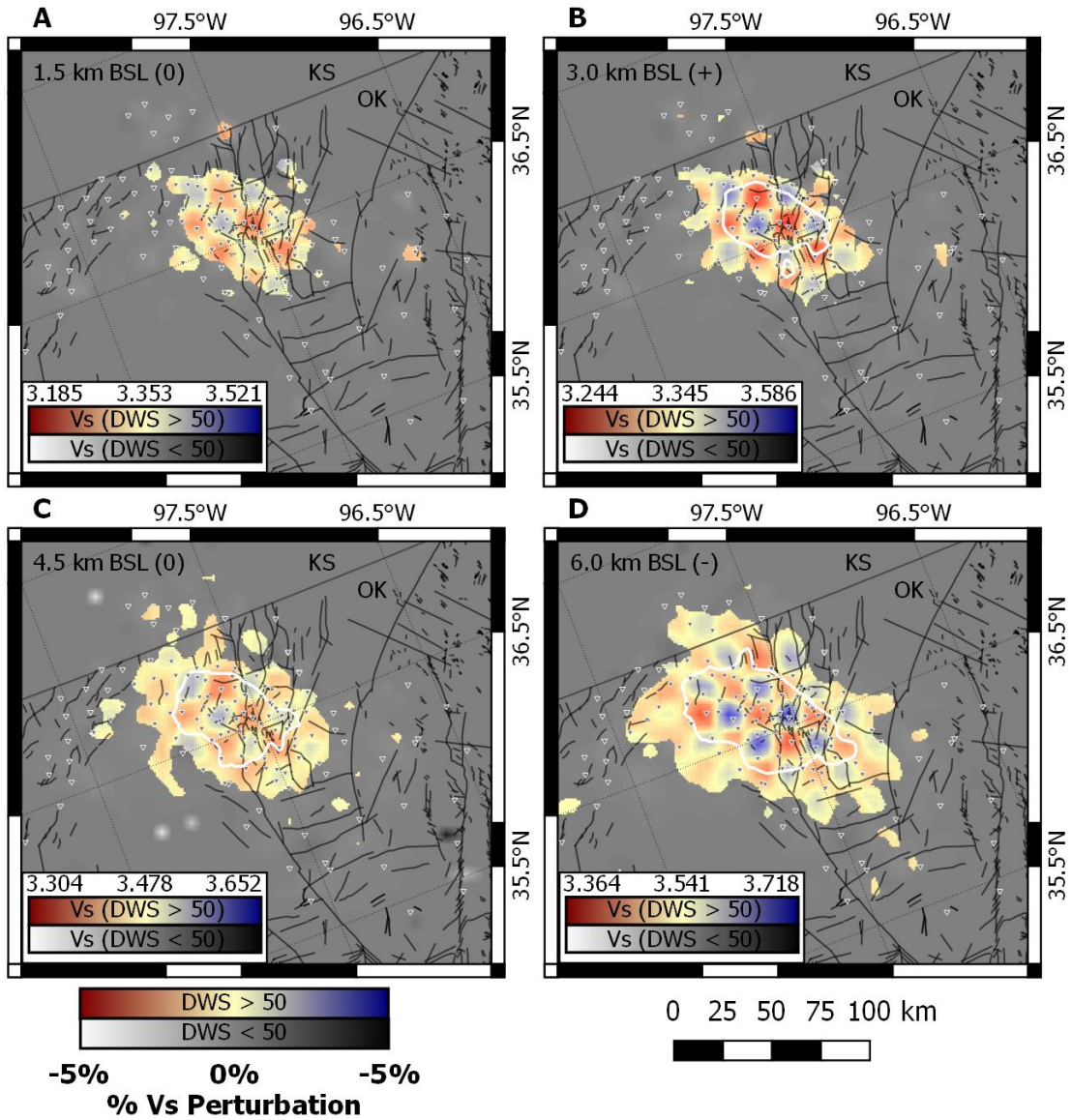


Figure 1.8: Shallow checkerboard recovery test results for Vs structure at the (A) 1.5 km, (B) 3.0 km, (C) 4.5 km, and (D) 6.0 km depth slices. The sign of imposed anomalies is shown in each figure corresponding to Figure 1.6.C. The transition from grayscale to colored results represents the DWS = 50 threshold, while the DWS = 150 threshold is represented by the white contour. Faults and political boundaries match Figure 1.1. Velocities in km/s.

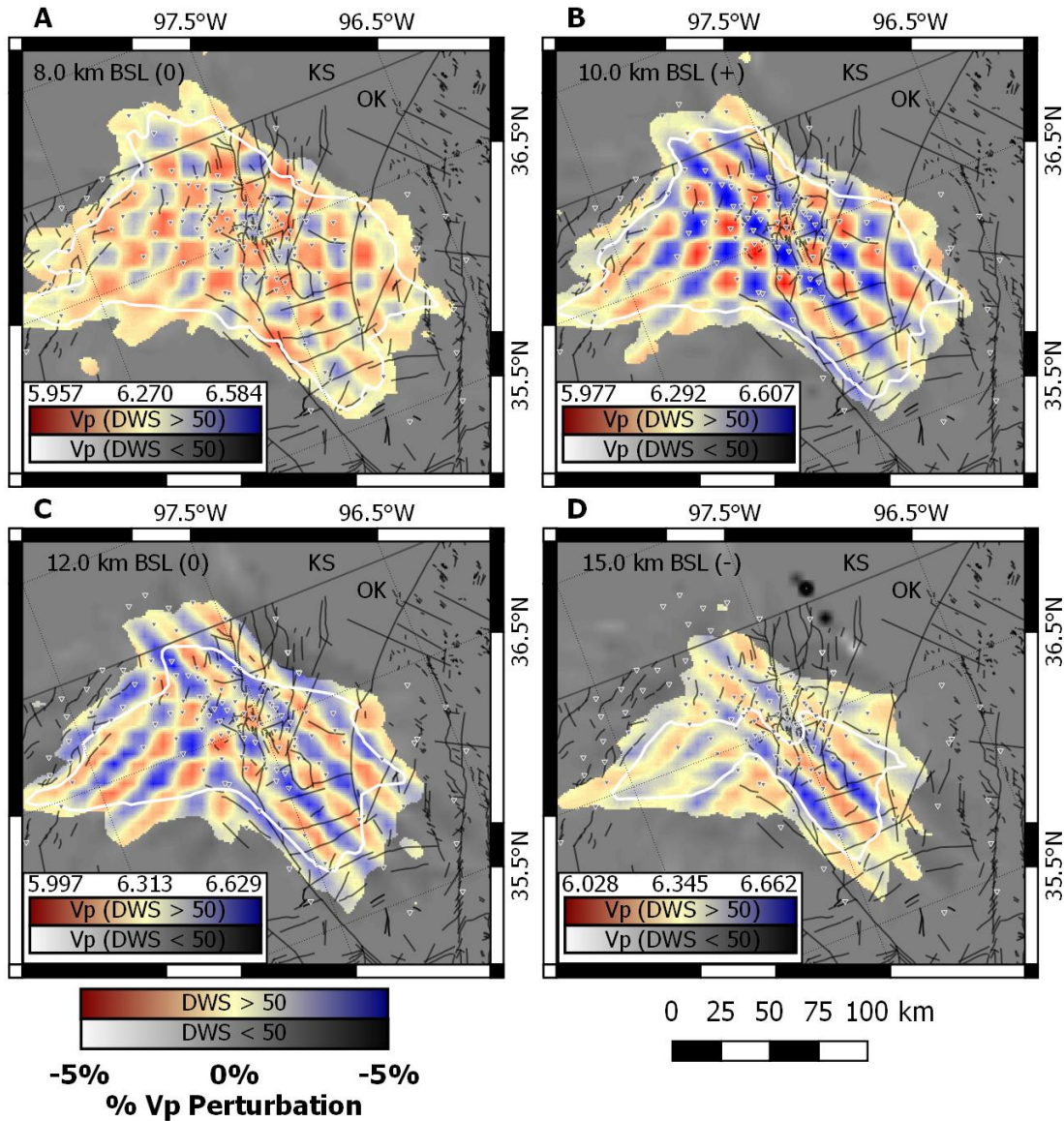


Figure 1.9: Deep checkerboard recovery test results for V_p structure at the (A) 8.0 km, (B) 10.0 km, (C) 12.0 km, and (D) 15.0 km depth slices. The sign of imposed anomalies is shown in each figure corresponding to Figure 1.6.C. The transition from grayscale to colored results represents the $DWS = 50$ threshold, while the $DWS = 150$ threshold is represented by the white contour. Faults and political boundaries match Figure 1.1. Velocities in km/s.

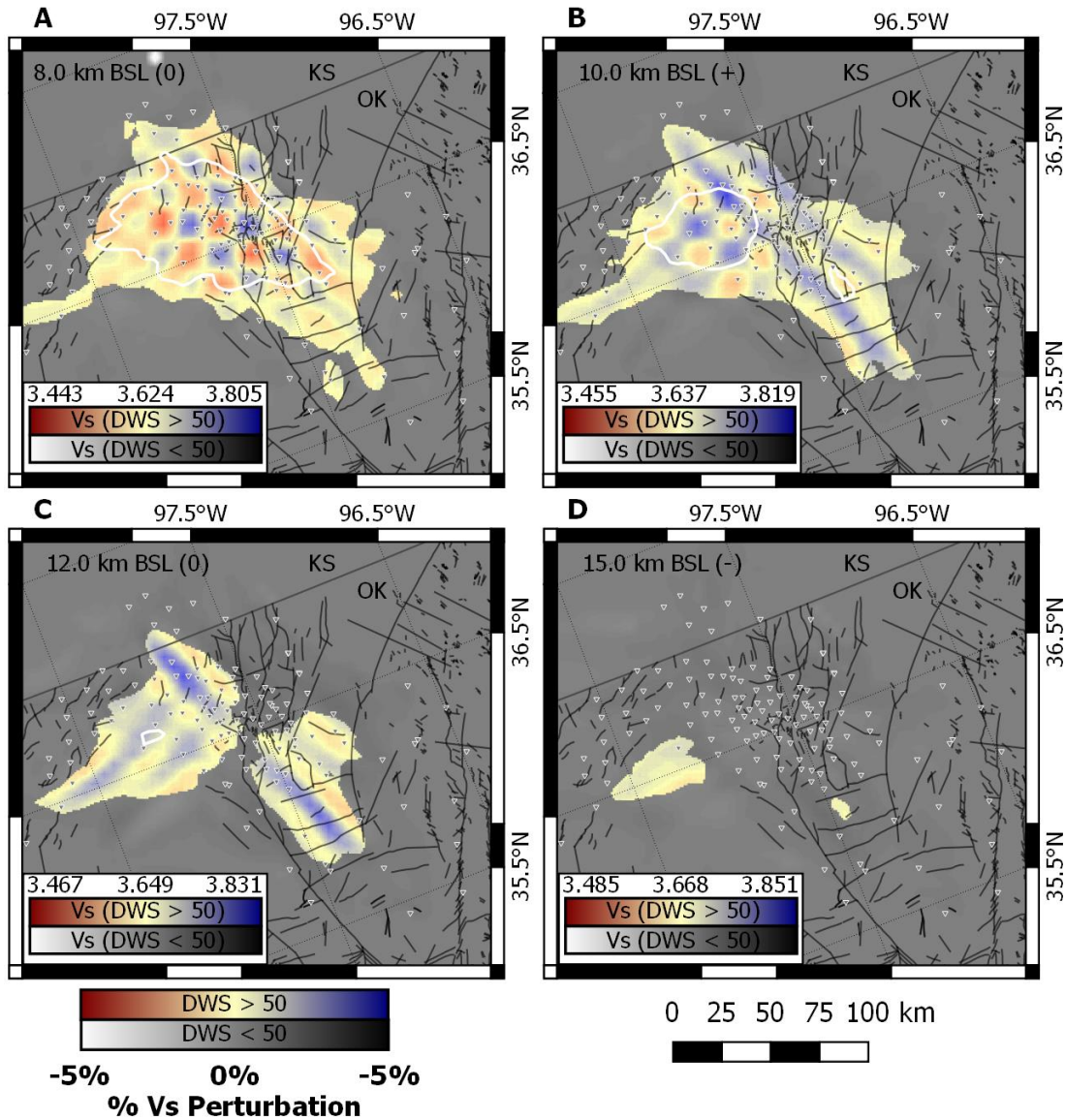


Figure 1.10: Deep Checkerboard recovery test results for Vs structure at the (A) 8.0 km, (B) 10.0 km, (C) 12.0 km, and (D) 15.0 km depth slices. The sign of imposed anomalies is shown in each figure corresponding to Figure 1.6.C. The transition from grayscale to colored results represents the DWS = 50 threshold, while the DWS = 150 threshold is represented by the white contour. Faults and political boundaries match Figure 1.1. Velocities in km/s.

Checkerboard test results at the 8.0 km depth slice again included no checkerboard structure in the input model (Figure 1.9.A); however, at $pDWS > 150$ recover perturbations of up to 1.1% (V_p range: 6.22–6.34 km/s) and up to 1.7% in V_s (V_s range: 3.58–3.68 km/s; Figure 1.10.A). Patterns in both V_p and V_s are similar to that of the imposed anomalies at 6.0 km BSL. Results at the 10.0 km depth slice, with an input checkerboard structure (Figure 1.9.B), recover up to 2.7% velocity perturbation. V_p ranges from 6.12 to 6.46 km/s. V_s results recover velocity perturbations up to 0.8% (V_s ranging from 3.62 km/s to 3.67 km/s).

V_p structure at the 12 km depth slice, which included no input checkerboard (Figure 1.9.C), recovers a checkerboard structure across a ~ 100 km by ~ 60 km region, consistent with the 10 km depth node checkerboard indicating downward smearing. ($pDWS > 150$). Recovered V_p values are as high as 6.48 km/s (a 2.7% perturbation), although velocities generally do not exceed values ranging from 6.20–6.41 km/s (1.7% perturbation). V_s recovery at 12 km depth (Figure 1.10.C) is unsuccessful, with very little area (~ 10 km by ~ 10 km) above the $sDWS > 150$ threshold. Recovery of V_p and V_s structures at 15 km (Figures 1.9.D and 1.10.D, respectively) is largely unsuccessful, with V_p structure showing significant lateral smearing, and very little of the V_s structure lying above the $sDWS > 50$ threshold.

Based upon checkerboard recovery test performance with the selected sub-catalog data, inversion results for V_p are well-resolved between 3.0 km and 8.0 km where sign, structure, and amplitude of imposed anomalies are recovered. Between 10–12 km, only sign and structure of anomalies are recovered. V_s structure is well-resolved between 3.0 km and 8.0 km, and only sign and structure of V_s perturbations

are considered in further analyses. Regions of well-recovered velocity sign and structure tend to correspond with DWS values greater than 150. These results suggest that low amplitude velocity anomalies of a scale 15 km by 15 km and larger, roughly the size of blocks within the Nemaha uplift, should be resolvable using the sub-catalog dataset and inversion scheme presented. Vertical smearing of imposed velocity anomalies are observed at depth nodes immediately adjacent to checkerboard layers, but the percent of the anomaly recovered in adjacent nodes is significantly less than the imposed anomalies. Lateral smearing is very limited within the $DWS > 150$ regions above the 10 km for both V_p and V_s recovery results and limited within the $150 > pDWS > 50$ region above 10 km BSL. Checkerboard recovery tests with spatially smaller anomalies were assessed, resulting in poor recovery of imposed V_p anomaly amplitudes (Figures 2.6-2.7) and imposed V_s anomalies at all depths (Figures 2.8-2.9).

Results: Inversion Performance with Observed Data

The root mean square (RMS) data residual for input data were reduced from 0.660 sec to 0.045 sec through this inversion. Of the 3103 input events, 2998 were relocated in the final iteration, representing a 3.4% attrition due to increasingly restrictive residual cutoffs in successive iterations (see full inversion solution control parameterization in Table 2.7; Appendix B). Event RMS location uncertainties were initially 497.5 m horizontally and 610.5 m vertically. Following inversion RMS location uncertainties were reduced to 81.3 m in the horizontal and 121.5 m in the vertical. Relocated earthquake locations are shown in Figure 1.11. Compressional and shear DWS structures from inversions using observed data are very similar to those

from the checkerboard recovery test. This supports use of identical DWS thresholds as resolution criteria for interpreting velocity structures recovered using observed data.

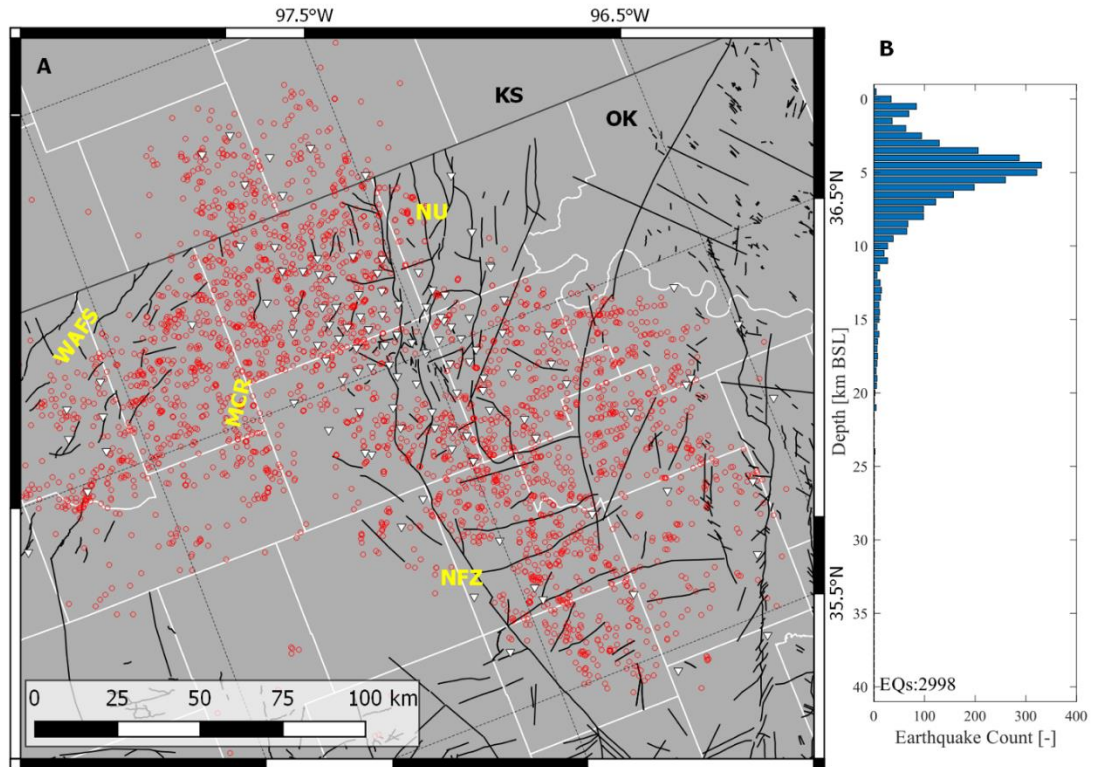


Figure 1.11: Relocated earthquake sub-catalog following TomoDD inversion. (A) Epicentral locations (red circles) are overlain on regional faults, features, and political boundaries (as in Figure 1.1). Station locations are shown as triangles. (B) Depth distribution and event count of the relocated earthquake sub-catalog.

Results: Compressional Velocity Structure

Depth slices of recovered compressional velocity structure between 3.0 km and 6.0 km BSL are shown in Figure 1.12 and 8.0 km and 12.0 km in Figure 1.13. At 3.0 km (Figure 1.12.A & D) V_p values are reduced along the Nemaha uplift within a 25 km by 50 km region, as well along the NFZ with values of 5.74 - 5.86 km/s (Figures 1.12.A & D). Small regions within the uplift have slightly enhanced velocities, from 5.92 - 6.04 km/s. V_p is elevated in the northeastern half of the MCR, ranging from

5.94 - 5.97 km/s. These values systematically decrease to values as low as 5.84 km/s within the MCR and as low as 5.78 km/s elsewhere.

Reduced V_p values persist in the Nemaha uplift at 4.5 km depth (Figures 1.12.B & E, initial V_p : 6.02 km/s), with values ranging from 5.86 km/s to 5.97 km/s across a ~25 km by ~60 km region and along the NFZ. V_p values are enhanced within one part of the uplift (a ~15 km by ~60 km region), across the MCR (a ~90 km by ~80 km region), and in a series of interconnected 20 km by 20 km regions in the uplift, with V_p values ranging from 6.00–6.16 km/s. The lower V_p continues into the 6 km depth slice (Figures 1.12.C & F, initial V_p : 6.13 km/s) with V_p values ranging from 6.02 – 6.10 km/s. The MCR at 6 km BSL shows a broad (80 km by 100 km) area with slightly enhanced V_p values (6.18–6.25 km/s) that extends into the western half of the Woods/Alfalfa counties region.

The 8.0 km and 10.0 km depth slices (Figures 1.13.A & B) show broadly reduced V_p across the resolved area, compared to the initial velocity model, with values ranging from 6.10 – 6.22 km/s (Figure 1.13.A & 1.13.B). The 12 km depth slice (Figure 1.13.C) shows a 60 km wide region with V_p values of 6.10–6.20 km/s coincident with the trend of the NFZ. The southwestern half of the MCR (100 km by 50 km area) shows enhanced V_p values of 6.30–6.36 km/s. Similar V_p enhancement is recovered to the east of the NFZ.

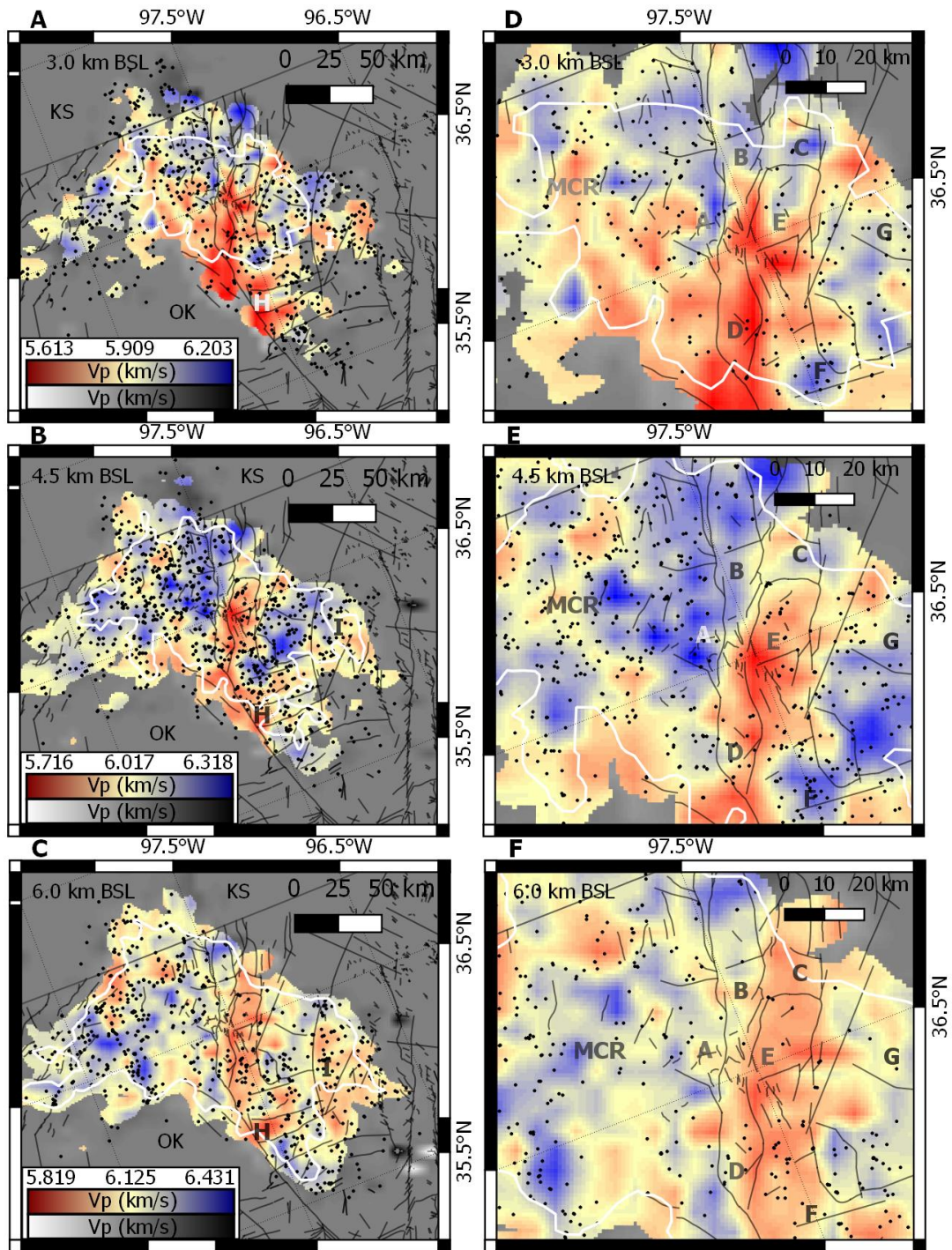


Figure 1.12: Recovered V_p structure at the (A) 3.0 km, (B) 4.5 km, and (C) 6.0 km depth slices. Hypocentral locations of the relocated sub-catalog events within 1/2 node spacing of each layer are projected onto depth slices (black dots). Detailed views of the Nemaha uplift are shown for the (D) 3.0 km, (E) 4.5 km, and (F) 6.0 km depth slices. Faults, labels, and political boundaries match Figure 1.1. Grayscale-color transitions and white contours represent the $pDWS = 50$ and 150 thresholds, respectively.

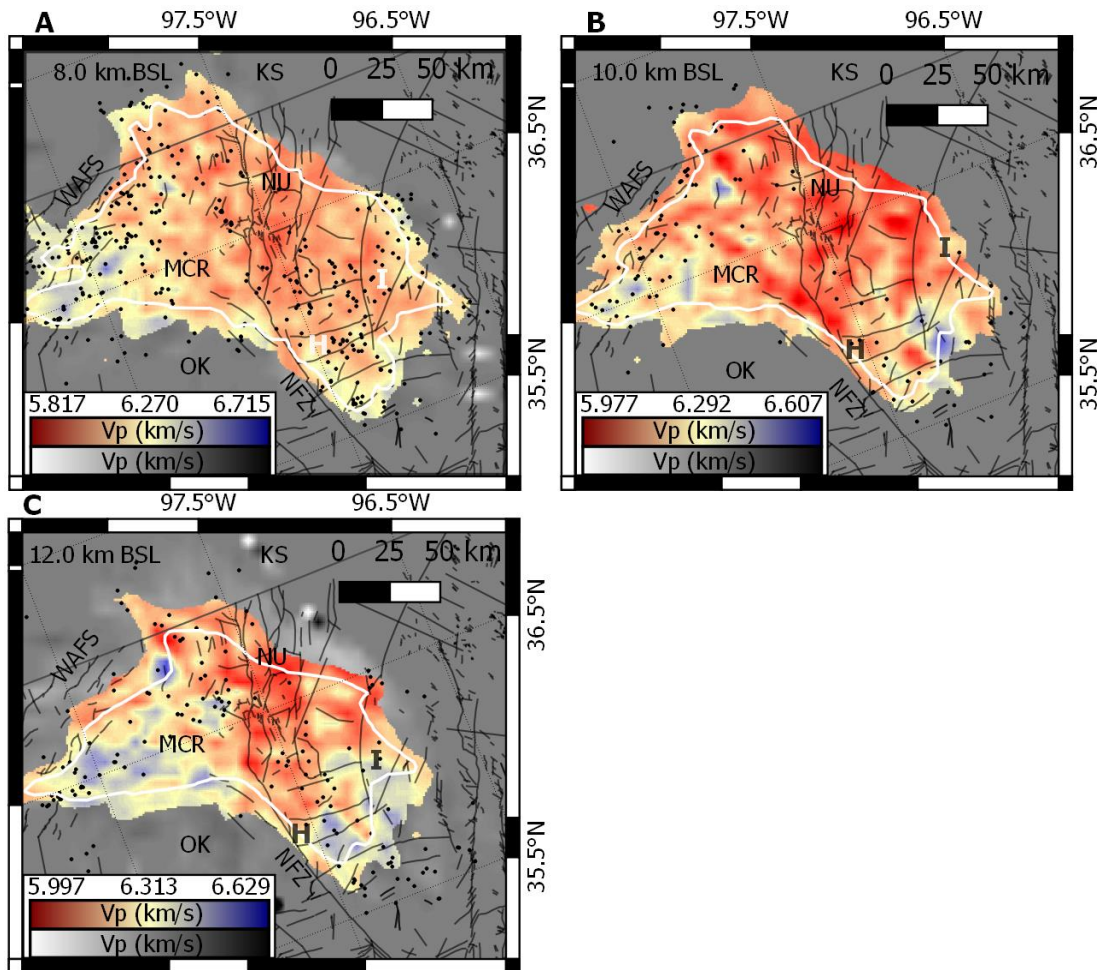


Figure 1.13: Recovered V_p structure at the (A) 8.0 km, (B) 10.0 km, and (C) 12.0 km depth slices. Hypocentral locations of the relocated sub-catalog events within 1/2 node spacing of each layer are projected onto depth slices (black dots). Faults, labels, and political boundaries match those of Figure 1.1. Grayscale-color transitions and white contours represent the $pDWS = 50$ and 150 thresholds, respectively.

Results: Shear Velocity Structure

Depth slices of recovered shear velocity structure between 3.0 and 8.0 km BSL are shown in Figures 1.14 and 1.15. The 3.0 km depth slice (Figures 1.14.A & C) has an initial V_s values of 3.42 km/s. The well-recovered region ($sDWS > 150$) encompasses a 60 km by 40 km ellipse, surrounded by a 90 km by 50 km partially-resolved ($sDWS > 50$) region. There is an overall SW to NE gradient in V_s values

with values as low as 3.40 km/s in the SW and as high as 3.46 km/s in the NE. There is a small, well-resolved region in the Nemaha uplift with Vs values as low as 3.30 km/s.

The 4.5 km depth slice (Figures 1.14.B & D) had an initial Vs value of 3.48 km/s. Blocks within the uplift show diminished values ranging from 3.39 to 3.44 km/s, as well as a 30 km wide, 60 km long swath across the MCR with values ranging from 3.44 – 3.47 km/s. Vs values are elevated (3.50-3.55 km/s) across much of the northeastern half of the MCR. Vs values are similarly enhanced to the northwest of the uplift, with sharp gradients consistent with mapped fault structures.

The 6 km depth slice (Figures 1.15.A & C) had an initial Vs value of 3.54 km/s. Blocks within the uplift continue to show diminished Vs (3.49 – 3.54 km/s), while other blocks have Vs values from 3.58 – 3.60 km/s. Transitions from diminished velocities in the uplift to enhanced velocities are consistent with mapped fault structure. The southeastern edge of the resolved region along the Woods/Alfalfa counties region shows Vs values of 3.52–3.54 km/s, and the southern half of the partially-resolved MCR has Vs values of 3.55 – 3.58 km/s.

The 8 km depth slice (Figures 1.15.B & D) had an initial Vs value of 3.62 km/s. The recovered depth slice shows Vs values of 3.57- 3.60 km/s across the entirety of the uplift. Vs is 3.58-3.60 km/s across the MCR, along the northeastern edge of the resolved region.

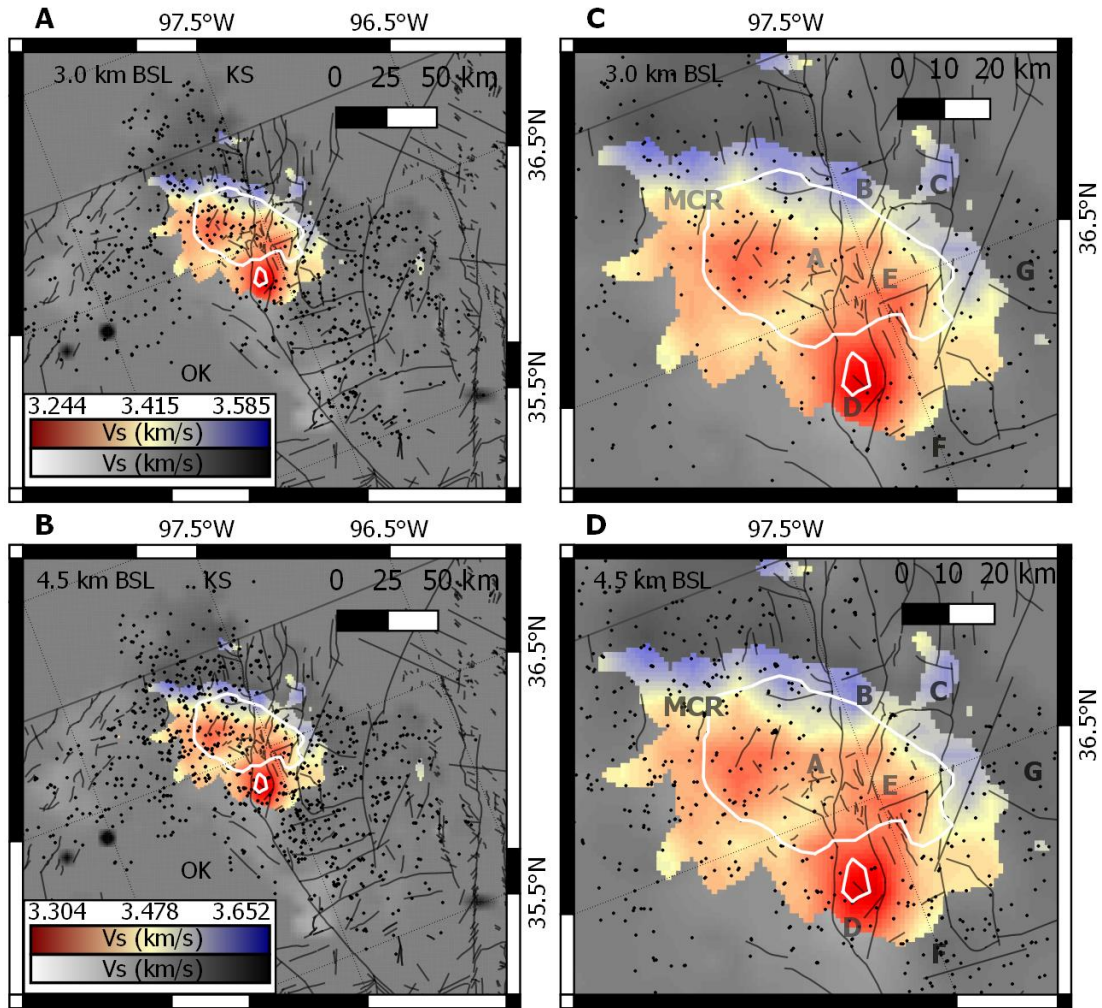


Figure 1.14: Recovered V_s structure at the (A) 3.0 km and (B) 4.5 km depth slices with detailed views of the (C) 3.0 km and (D) 4.5 km slices about the Nemaha uplift. Hypocentral locations of the relocated sub-catalog events within 1/2 node spacing of each layer are projected onto depth slices (black dots). Faults and political boundaries match Figure 1.1. Grayscale-color transitions and white contours represent the $sDWS = 50$ and 150 thresholds, respectively.

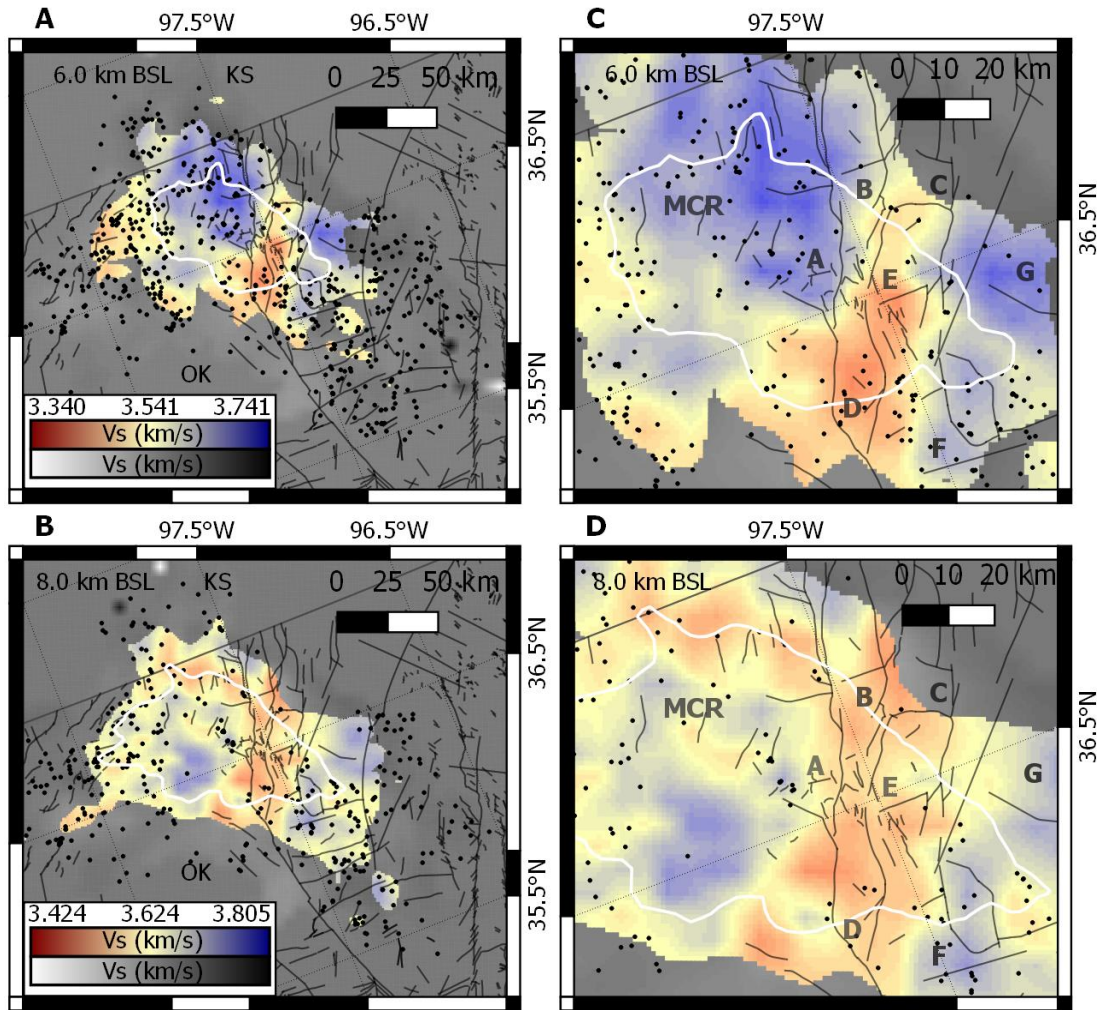


Figure 1.15: Recovered V_s structure at the (A) 6.0 km and (B) 8.0 km depth slices with detailed views of the (C) 6.0 km and (D) 8.0 km slices about the Nemaha uplift. Hypocentral locations of the relocated sub-catalog events within 1/2 node spacing of each layer are projected onto depth slices (black dots). Faults and political boundaries match Figure 1.1. Grayscale-color transitions and white contours represent the $sDWS = 50$ and 150 thresholds, respectively.

Discussion: Vp/Vs Structure

There is enough difference in the resolution quality of Vp and Vs structure as to significantly impact the accurate estimation of Vp/Vs structure via direct division. Therefore, Vp/Vs structure is not extensively discussed here, but is documented for all simulations referenced in Appendix B. Vp/Vs values may be slightly elevated within the Nemaha uplift compared to neighboring regions, which could provide further indication of increased fracture density across the uplift (e.g., Moos & Zoback, 1983). This possibility warrants further investigation using an inversion method that directly inverts for Vp/Vs.

Discussion: Faulting, Seismicity, and Basement Hydrology

High-rate SWD has been linked to seismicity tens of kilometers away from injection sources in this region through hydrologic connectivity in the Arbuckle Group and crystalline basement (e.g., Keranen et al., 2014; Yeck et al., 2016; Hincks et al., 2018). As faults develop in crystalline rocks, permeability and porosity throughout the damage zone are enhanced (Brace, 1980; Mitchell & Faulkner, 2012). Fault networks in the NFZ and in the Woods/Alfalfa counties region are likely more interconnected than those in regions without faults expressed in the sedimentary cover. Increased fracture connectivity potentially limits pore fluid pressurization from injection, resulting in the observed relative aseismicity in the uplift. In comparison, regions where fault networks are less interconnected, lower permeability may lead to local increases in pore fluid pressure and possible seismicity.

Discussion: Compressional Velocity Structure, Seismicity, and Fault Distributions

Recovered V_p values are 0.16-0.52 km/sec lower than values expected for intact granite at shallow crustal depths (6.16-6.29 km/s for 5-10 km depth; Christensen et al., 1995), likely resulting from extensive faulting and weathering of the uppermost crust in this region (Denison, 1981; Moos & Zoback, 1983; Boadu & Long, 1996; Schwing et al., 2016; Hamilton et al., 2017; Morgan et al., 2017). Values are not as low as those of near-surface samples of heavily damaged granites from southern Oklahoma (4.5-5.0 km/sec, after Katz et al., 2001; Katz & Reches, 2004). Recovered values are consistent with previous tomographic studies, which show broad regions of reduced V_p (0.1-0.3 km/sec reduction) across the region. Recovered V_p anomalies in this study fall within this range but reveal lateral heterogeneities on the scale of tens of kms that are spatially coherent with known patterns of faulting (Figure 1.12). V_p values are reduced by 0.1-0.3 km/sec within much of the Nemaha uplift and along the NFZ, while velocities across much of the MCR are enhanced by 0.1-0.3 km/sec between 3 and 6 km depth. V_p enhancement on either side of the uplift is roughly even within these depth slices, suggesting similar lithologies and fracture densities in the uppermost crust across these sub-regions. At greater depths (particularly at 12 km, Figure 1.13.C) there are some indications of enhanced V_p within the MCR that are consistent with hypothesized mafic intrusions interpreted from earlier regional tomography (Chen, 2016). These deeper, enhanced V_p regions are at the edge of established resolution thresholds.

The NE-SW velocity gradient observed in shallow V_p results (3km, Figures 1.12.A & D) is consistent with the overall structural trend between the Cherokee Platform (this study area) and the Anadarko basin to the southwest. This trend may reflect increased fracture density in basement rock closer to the sediment-basement interface. Alternatively, it may represent a reduction in the average recovered velocity

due to a greater sedimentary cover component being averaged into nodes at the 1.5 km and 3.0 km depths in the southwest.

Relocated patterns of seismicity are largely concentrated in the upper 5 km of the crust (3-8 km BSL) and tend to lie within regions of enhanced V_p outside the Nemaha uplift. Within the uplift this trend varies, with seismicity at the periphery of reduced V_p regions. These may represent a transition zone between regions of increased fracture density and those with lower fracture density where pore fluid pressures may increase. At greater depths, earthquake locations tend to concentrate near areas with mapped faulting (see Figure 1.13).

Discussion: Shear Velocity Structure and Fault Distribution

Recovered shear velocity structure indicates an apparent correlation between reduced V_s , major fault-bounded structures, and zones of relative aseismicity in the upper crust (3-8 km BSL, compare Figures 1.12 and 1.15). These spatial relationships may suggest enhanced fluid volume within more-extensively faulted regions of the upper crust. Increased fault density in these regions, based upon mapped fault density from Marsh & Holland (2016), would result in increased porosity and permeability of the crystalline basement. High porosity and permeability could reduce pore fluid pressure under uniform injection rates and may reduce the likelihood of induced events within these regions. This conceptual model is consistent with observations of limited seismic activity within regions of mapped faulting near large SWD wells (Lambert, 2017). Active seismic lineaments within the Nemaha uplift may reflect local pressurization; such features are smaller than the limit of resolution for V_s structure. Outside regions of mapped faulting, the correlation between recovered V_s structure seismicity distribution weakens.

Discussion: Hypothesis of Compartmentalization in the Nemaha Uplift

Tomography and hypocentral relocation results recover elevated, localized V_p and V_s values in conjunction with very limited seismicity in fault-bounded blocks within the Nemaha uplift (Figures 1.12-1.15). Similar V_p values are recovered to the west of the uplift, but with extensive seismic activity (see Figures 1.12 and 1.13). V_s is also elevated in these blocks compared to the rest of the uplift (Figures 1.14 and 1.15). Faults bounding these blocks have hundreds of meters of throw, which may isolate the hydrologic system of the block from surrounding regions (Gay, 2003a, 2003b; Higley et al., 2014; Marsh and Holland, 2016). This motivates the hypothesis that the limited seismicity and enhanced V_p and V_s in fault-bounded blocks may represent hydrological compartmentalization or a marked decrease in the fracture density and fluid volume within small regions.

Conclusions

This thesis presents a new, high-resolution 3-D velocity model for the shallow crust in north-central Oklahoma using results from a recent dense seismic deployment, enabling a 2-4-fold increase in model resolution compared to previous studies (Chen, 2016; Pei et al., 2018). Compressional (V_p) and shear (V_s) velocity structures are resolved at length scales of 15 km for small velocity variations (< 0.4 km/s for V_p and < 0.2 km/s for V_s) within in the upper crust (3.0–8.0 km BSL). Recovered V_p structure displays strong spatial correlation with known patterns of faulting and fault-bounded blocks within the Nemaha uplift, particularly in its eastern and southern blocks. Similar V_p reductions are recovered in central Oklahoma along the trace of the Nemaha Fault Zone and in adjacent fault-bounded blocks. Variations in V_p structure are interpreted as relative fracture density in the shallow crust rather than variations in lithology. Weathering along faults likely contributes to velocity values recovered at

these depths (Schwing et al., 2016; Hamilton et al., 2017). At greater depths (8-12 km BSL) recovered V_p structure is similar to those of earlier tomography studies (Chen, 2016; Pei et al., 2018) and are consistent with expected lithologies (Katz & Reches, 2004; Shah & Keller, 2017). Recovered V_s structure in the upper crust (3-8 km BSL) shows possible correlation with regions of mapped faulting and patterns of seismicity. These results possibly represent enhanced fluid volume in the crust and more interconnected fracture networks associated with regions of extensive mapped faulting. The extensive mapped faulting and relative seismic quiescence of the Nemaha uplift may indicate that pore fluid pressures are reduced in these regions. This may be due to enhanced porosity and permeability from increased density and interconnectivity of faults within mapped structures, compared to fault networks illuminated by seismicity alone. Recovered patterns of velocity and seismicity presented here may serve as a groundwork for estimating relative hydrologic parameters in future studies.

REFERENCES

- Alt, R. C. J., & Zoback, M. D. (2017). In Situ Stress and Active Faulting in Oklahoma. *Bulletin of the Seismological Society of America*, 107(1), 1–13. <https://doi.org/10.1785/0120160156>
- Boadu, F. K., & Long, L. T. (1996). Effects of fractures on seismic-wave velocity and attenuation. *Geophysical Journal International*, 127, 86–110.
- Brace, W. F. (1980). Permeability of crystalline and argillaceous rocks. *International Journal of Rock Mechanics and Mining Sciences and Geomechanics*, 17(5), 241–251. [https://doi.org/10.1016/0148-9062\(80\)90807-4](https://doi.org/10.1016/0148-9062(80)90807-4)
- Chen, C. (2016). *Comprehensive Analysis of Oklahoma Earthquakes : From Earthquake Monitoring to 3D Tomography and Relocation*. University of Oklahoma.
- Christensen, N. I. (1996). Poisson’s ratio and crustal seismology. *Journal of Geophysical Research: Solid Earth*, 101(B2), 3139–3156. <https://doi.org/10.1029/95JB03446>
- Christensen, N. I., Mooney, W. D., & Christensen, N.I., Mooney, W. D. (1995). Seismic velocity structure and composition of the continental crust: A global view. *Journal of Geophysical Research: Solid Earth (1978–2012)*, 100(B6), 9761–9788. <https://doi.org/10.1029/95JB00259>
- Darold, A. P., Holland, A. A., Jennifer, K., & Gibson, A. R. (2015). Oklahoma Earthquake Summary Report 2014. *Oklahoma Geological Survey Open File Report, OF1-2015*, 1–46. Retrieved from http://ogs.ou.edu/pubsscanned/openfile/OF1_2015.pdf
- Denison, R. E. (1981). Basement Rocks in Northeastern Oklahoma. *Oklahoma Geological Survey Circular*, 84.
- Dunn, M., DeShon, H. R., & Powell, C. A. (2013). Imaging the New Madrid Seismic Zone using double-difference tomography. *Journal of Geophysical Research: Solid Earth*, 118(10), 5404–5416. <https://doi.org/10.1002/jgrb.50384>
- Eberhart-phillips, D. (1986). Three-Dimensional Velocity Structure in Northern California Coast Ranges From Inversion of Local Earthquake Arrival Times. *Bulletin of the Seismological Society of America*, 76(4), 1025–1052.
- Ellsworth, W. L. (2013). Injection-Induced Earthquakes. *Science*, 341(6142), 1–8. <https://doi.org/10.1126/science.1225942>
- Frohlich, C., Hayward, C., Stump, B., & Potter, E. (2011). The Dallas-Fort Worth earthquake sequence: October 2008 through May 2009. *Bulletin of the Seismological Society of America*, 101(1), 327–340. <https://doi.org/10.1785/0120100131>
- Gay, S. P. J. (2003a). The Nemaha Trend-A System of Compressional Thrust-Fold, Strike-Slip Structural Features in Kansas and Oklahoma (Part 2, Conclusion). *Shale Shaker*, 54(2), 39–49.
- Gay, S. P. J. (2003b). The Nemaha Trend - A system of compressional thrust-fold strike-slip structural features in Kansas and Oklahoma, Part 1. *Shale Shaker*, 54(1), 9–17.
- Hamilton, M., Evans, S., Engel, M. H., & Elmore, D. (2017). Evidence for Deep Fluid Penetration into the Precambrian Basement, Oklahoma. In *GSA Annual Meeting2*. Seattle, WA: The Geological Society of America. Retrieved from <https://gsa.confex.com/gsa/2017AM/webprogram/Paper303870.html>
- Higley, D. K., Gianoutsos, N. J., Pantea, M. P., & Strickland, S. M. (2014). Precambrian to Ground Surface Grid Cell Maps and 3D Model of the Anadarko

- Basin Province. In D. K. Higley (Ed.), *Petroleum systems and assessment of undiscovered oil and gas in the Anadarko Basin Province, Colorado, Kansas, Oklahoma, and Texas—USGS Province 58: U.S. Geological Survey Digital Data Series DDS-69-EE* (p. 8). U.S. Geological Survey.
<https://doi.org/http://dx.doi.org/10.3133/ds69EE>
- Hincks, T., Aspinall, W., Cooke, R., & Gernon, T. (2018). Oklahoma's induced seismicity strongly linked to wastewater injection depth. *Science*, *1255*(March), 1251–1255.
- Horton, S. (2012). Disposal of Hydrofracking Waste Fluid by Injection into Subsurface Aquifers Triggers Earthquake Swarm in Central Arkansas with Potential for Damaging Earthquake. *Seismological Research Letters*, *83*(2), 250–260. <https://doi.org/10.1785/gssrl.83.2.250>
- Katz, O., & Reches, Z. (2004). Microfracturing, damage, and failure of brittle granites. *Journal of Geophysical Research: Solid Earth*, *109*(B1), 1–13.
<https://doi.org/10.1029/2002JB001961>
- Katz, O., Gilbert, M. C., Reches, Z., & Roegiers, J.-C. (2001). Mechanical Properties of the Mount Scott Granite, Wichita Mountains, Oklahoma. Oklahoma Geological Survey.
- Keranen, K. M., Savage, H. M., Abers, G. A., & Cochran, E. S. (2013). Potentially induced earthquakes in Oklahoma, USA: Links between wastewater injection and the 2011 Mw5.7 earthquake sequence. *Geology*, *41*(6), 699–702.
<https://doi.org/10.1130/G34045.1>
- Keranen, K. M., Weingarten, M., Abers, G. A., Bekins, B. A., & Ge, S. (2014). Sharp increase in central Oklahoma seismicity since 2008 induced by massive wastewater injection. *Science*, *345*(6195), 448–451.
<https://doi.org/10.1126/science.1255802>
- Kim, W. Y. (2013). Induced seismicity associated with fluid injection into a deep well in Youngstown, Ohio. *Journal of Geophysical Research: Solid Earth*, *118*(7), 3506–3518. <https://doi.org/10.1002/jgrb.50247>
- Lambert, C. E. (2017). *Structural Controls on Fluid Migration and Seismic Variability in Northern Oklahoma*. Cornell University.
- Marsh, S., & Holland, A. (2016). Comprehensive Fault Database and Interpretive Fault Map of Oklahoma. *Oklahoma Geological Survey Open File Report OF2-2016*.
- McNamara, D. E., Benz, H. M., Herrmann, R. B., Bergman, E. A., Earle, P., Holland, A., et al. (2015). Earthquake hypocenters and focal mechanisms in central Oklahoma reveal a complex system of reactivated subsurface strike-slip faulting. *Geophysical Research Letters*, *42*(8), 2742–2749.
<https://doi.org/10.1002/2014GL062730>
- Mitchell, B. J., & Landisman, M. (1970). Interpretation of a crustal section across Oklahoma. *Bulletin of the Geological Society of America*, *81*(9), 2647–2656.
[https://doi.org/10.1130/0016-7606\(1970\)81\[2647:IOACSA\]2.0.CO;2](https://doi.org/10.1130/0016-7606(1970)81[2647:IOACSA]2.0.CO;2)
- Mitchell, T. M., & Faulkner, D. R. (2012). Towards quantifying the matrix permeability of fault damage zones in low porosity rocks. *Earth and Planetary Science Letters*, *339–340*, 24–31. <https://doi.org/10.1016/j.epsl.2012.05.014>
- Moos, D., & Zoback, M. D. (1983). In situ studies of velocity in fractured crystalline rocks. *Journal of Geophysical Research: Solid Earth*, *88*(B3), 2345–2358.
<https://doi.org/10.1029/JB088iB03p02345>
- Moos, D., & Zoback, M. D. (1983). In Situ Studies of Velocity in Fractured Crystalline Rocks. *JGR*, *88*(B3), 2345–2358.
- Morgan, C., Johnson, C. S., Carpenter, B. M., & Reches, Z. (2017). Structural and Geophysical Characterization of Oklahoma Basement. *AGU Fall Meeting*, S23C–

0839.

- Pei, S., Peng, Z., & Chen, X. (2018). Locations of injection-induced earthquakes in Oklahoma controlled by crustal structures. *Journal of Geophysical Research: Solid Earth*. <https://doi.org/10.1002/2017JB014983>
- Schoenball, M., & Ellsworth, W. L. (2017a). A Systematic Assessment of the Spatiotemporal Evolution of Fault Activation Through Induced Seismicity in Oklahoma and Southern Kansas. *Journal of Geophysical Research: Solid Earth*, 122(12), 10,189–10,206. <https://doi.org/10.1002/2017JB014850>
- Schoenball, M., & Ellsworth, W. L. (2017b). Waveform-Relocated Earthquake Catalog for Oklahoma and Southern Kansas Illuminates the Regional Fault Network. *Seismological Research Letters*, 88(5), 1252–1258. <https://doi.org/10.1785/0220170083>
- Schwing, J. E., Evans, S., Ellmore, R. D., Engel, M. H., & Hein, B. (2016). Alteration of Basement Rocks in Oklahoma by Fluid Interactions. In *GSA Annual Meeting* (Vol. 201–3). Denver, CO. Retrieved from <https://gsa.confex.com/gsa/2016AM/webprogram/Paper286362.html>
- Shah, A. K., & Keller, G. R. (2017). Geologic influence on induced seismicity: Constraints from potential field data in Oklahoma. *Geophysical Research Letters*, 44, 152–161. <https://doi.org/10.1002/2016GL071808>
- Thurber, C. H., Brocher, T. M., Zhang, H., & Langenheim, V. E. (2007). Three-dimensional P wave velocity model for the San Francisco Bay region, California. *Journal of Geophysical Research*, 112(B7), B07313. <https://doi.org/10.1029/2006JB004682>
- Toomey, D. R., & Foulger, G. R. (1989). Tomographic inversion of local earthquake data from the Hengill-Grensdalur Central Volcano Complex, Iceland. *Journal of Geophysical Research*, 94(B12), 17497. <https://doi.org/10.1029/JB094iB12p17497>
- Tryggvason, R., & Qualls, B. R. (1967). Seismic Refraction Measurements of Crustal Structure in Oklahoma. *Journal of Geophysical Research*, 72(14), 3738–3740. <https://doi.org/10.1029/JZ072i014p03738>
- Um, J., & Thurber, C. (1987). Fast Algorithm for Two-Point Seismic Ray Tracing. *Bulletin of the Seismological Society of America*, 77(3), 972–986.
- Waldhauser, F., & Ellsworth, W. L. (2000). A Double-difference Earthquake location algorithm: Method and application to the Northern Hayward Fault, California. *Bulletin of the Seismological Society of America*, 90(6), 1353–1368. <https://doi.org/10.1785/0120000006>
- Watkins, W. D., Thurber, C. H., Abbott, E. R., Brudzinski, M., & Grand, S. P. (2018). Local earthquake velocity and attenuation tomography of the Jalisco, Mexico region. *Tectonophysics*. <https://doi.org/10.1016/j.tecto.2018.01.002>
- Weingarten, M., Ge, S., Godt, J. W., Bekins, B. A., & Rubinstein, J. L. (2015). High-rate injection is associated with the increase in U.S. mid-continent seismicity. *Science*, 348(6241), 1336–1340. <https://doi.org/10.1126/science.aab1345>
- Withers, M., Aster, R., Young, C., Beiriger, J., Harris, M., Moore, S., & Trujillo, J. (1998). A comparison of select trigger algorithms for automated global seismic phase and event detection. *Bulletin of the Seismological Society of America*, 88(1), 95–106. <https://doi.org/10.1029/2012JD017694>
- Yeck, W. L., Weingarten, M., Benz, H. M., McNamara, D. E., Bergman, E. A., Herrmann, R. B., et al. (2016). Far-field pressurization likely caused one of the largest injection induced earthquakes by reactivating a large preexisting basement fault structure. *Geophysical Research Letters*, 43(19), 10,198–10,207. <https://doi.org/10.1002/2016GL070861>
- Zhang, H., & Thurber, C. H. (2003). Double-difference tomography: The method and

- its application to the Hayward Fault, California. *Bulletin of the Seismological Society of America*, 93(5), 1875–1889. <https://doi.org/10.1785/0120020190>
- Zhang, H., & Thurber, C. H. (2006). Development and applications of double-difference seismic tomography. *Pure and Applied Geophysics*, 163, 373–403. <https://doi.org/10.1007/s00024-005-0021-y>
- Zhang, H., & Thurber, C. H. (2007). Estimating the model resolution matrix for large seismic tomography problems based on Lanczos bidiagonalization with partial reorthogonalization. *Geophysical Journal International*, 170(1), 337–345. <https://doi.org/10.1111/j.1365-246X.2007.03418.x>
- Zhang, H., Sarkar, S., Toksoz, M. N., & Kuleli, H. S. (2009). Passive Seismic Tomography Using Induced Seismicity at a Petroleum Field in Oman, 74(6).
- Zhu, H. (2018). Crustal wavespeed structure of North Texas and Oklahoma based on ambient noise cross-correlation functions and adjoint tomography. *Geophysical Journal International*. <https://doi.org/10.1093/gji/ggy169>

CHAPTER 2

SUPPLEMENTARY MATERIALS

XR Network Deployment Methods

Due to the flat-lying topography of many of the station locations in the XR network, several locations were at increased risk of periods of immersion during storm seasons in Oklahoma. These sites were equipped with a “double-walled” seismometer vault capable of draining. The double-walled vault design consisted of a 44-gallon trash can with its bottom removed acted as an outer vault, maintaining an air-gap between the ground and the inner vault. The inner vault consisted of an inverted, rigid plastic container that acted as a dive-bell, isolating the instrument in a pocket of air during inundation (Figure 2.1). The inner vault was secured by a compression rope (Figure 2.1) to eye-bolts mounted in a small (15 cm by 20 cm wide) concrete pier on which the seismometer rested. Piers were anchored into the ground with metal cleats (Figure 2.2) to prevent pier dislodgement and improve instrument coupling. Following installation of the pier, pea-sized gravel was poured around the pier to encourage drainage (Figure 2.1).



Figure 2.1: Inner vault installed over a CMG-3T instrument. The ropes shown here have 3 tiers of tension knots to prevent loosening or dislodgement of the inner vault in the event of inundation.



Figure 2.2: Double-walled vault pier hardware prior to pouring concrete. Cleats are driven into the pilot holes in the underlying soil to ensure sufficient penetration depth to prevent pier dislodgement.

To reduce cultural noise and prevent site vandalism, most stations were located near the center of 1 mile by 1 mile “sections”, often without road access. Lighter, single-walled seismometer vaults were devised for these locations, which relied upon being placed in well-drained areas and a water-tight design. 30-gallon concrete-mixing barrels (Figure 2.3) with water-tight lids were used for this purpose, and retro-fitted with an inverted P-trap on the lid to prevent water entry through the sensor-cable port. The barrels were cemented in place and tied to the cement pad with embedded anchors and rope on the outside of the barrel to prevent decoupling of the barrel from the earth in the event of an elevated ground-water table (Figure 2.3, point A). A thin (<10 cm) cement pad was poured and leveled inside the barrel to provide a platform for the installed instrument. The sealing gasket in the barrels’ lids were further augmented with plumbing putty to reduce the likelihood inundation. The single wall vaults were anchored to a concrete slab to prevent



Figure 2.3: Installed single-wall vault with the PVC P-trap sensor cable conduit and lid approximately 5 cm above grade.

The single-wall vault P-trap assembly was constructed of 2-inch outer diameter PVC components that would still allow passage of a sensor cable without undue trouble. Each PVC joint was sealed using primer and PVC glue, and a 2-inch to 1.5-inch coupling was attached to the outgoing end of the assembly to limit ingress of water, animals, or soil. This was later sealed with the plastic sheathing placed around the sensor cable. The P-trap assembly was mounted to the vault lid through a hole made with a 2-inch hole-saw. The juncture between the lid and P-trap assembly was sealed by flooding it with LocTite© Plastics Bonder. This cyanoacrylate glue is brittle, and therefore was structurally re-enforced with PVC collars and rubber-cement on either side of the lid to limit strain on the glue/seal. Of the 35 stations in the XR network that used this vault design, only two shows signs of water-entry at the end of a 1.5-year deployment that included two storm seasons.

Station boxes were built from 30-gallon HDPE storage boxes. These were sufficiently light-weight, durable, and animal resistant for this deployment. Additionally, they served as a safe containment vessel for the two cases where lead-acid battery casings became compromised during the XR deployment. Each box was fitted with a cable port through which the sensor, GPS, and solar-panel cables were routed. These cables were encased in plastic and steel hardware-cloth to prevent damage from elements and animals. The cable ports were stuffed with steel-wool to prevent rodent colonization. Between service-runs station box lids were sealed with plumbing putty and industrial duct-tape along the lid lip to prevent water ingress and subsequently wrapped in tarp material to prevent sun damage to the station box. Each box was placed inside the frame of the solar-panel (Figure 2.3) to supplement the anchors holding the solar-panel in place.

Alternative Input Catalog & Velocity Model Inversion Results

A series of velocity model perturbations to the initial velocity model (Figure 1.3.A) were assessed to investigate inversion sensitivity to the input model. Results from two end-member test where the initial model was perturbed by $\pm 5\%$ are shown in Figure 2.4. Results for the increased seismic velocity inversion results in similar structures in V_p and V_s as those of the initial velocity model (compare Figure 2.4.A & D to Figures 1.12.C and 1.14.C). Reduction of the initial velocity model results in recovery of similar broad velocity structure (compare Figure 2.4.B & 2.4.E to Figure 1.12.C and 1.14.C). An alternative input earthquake catalog, consisting of 8629 events, was assessed using the standard initial velocity model (Darold et al., 2015). Inversion results using this “dense” input catalog (Figure 2.4.C) produced similar results to those of the best-fit inversion analyzed in Chapter 1. The distribution of events for the dense catalog are shown in Figure 2.5.

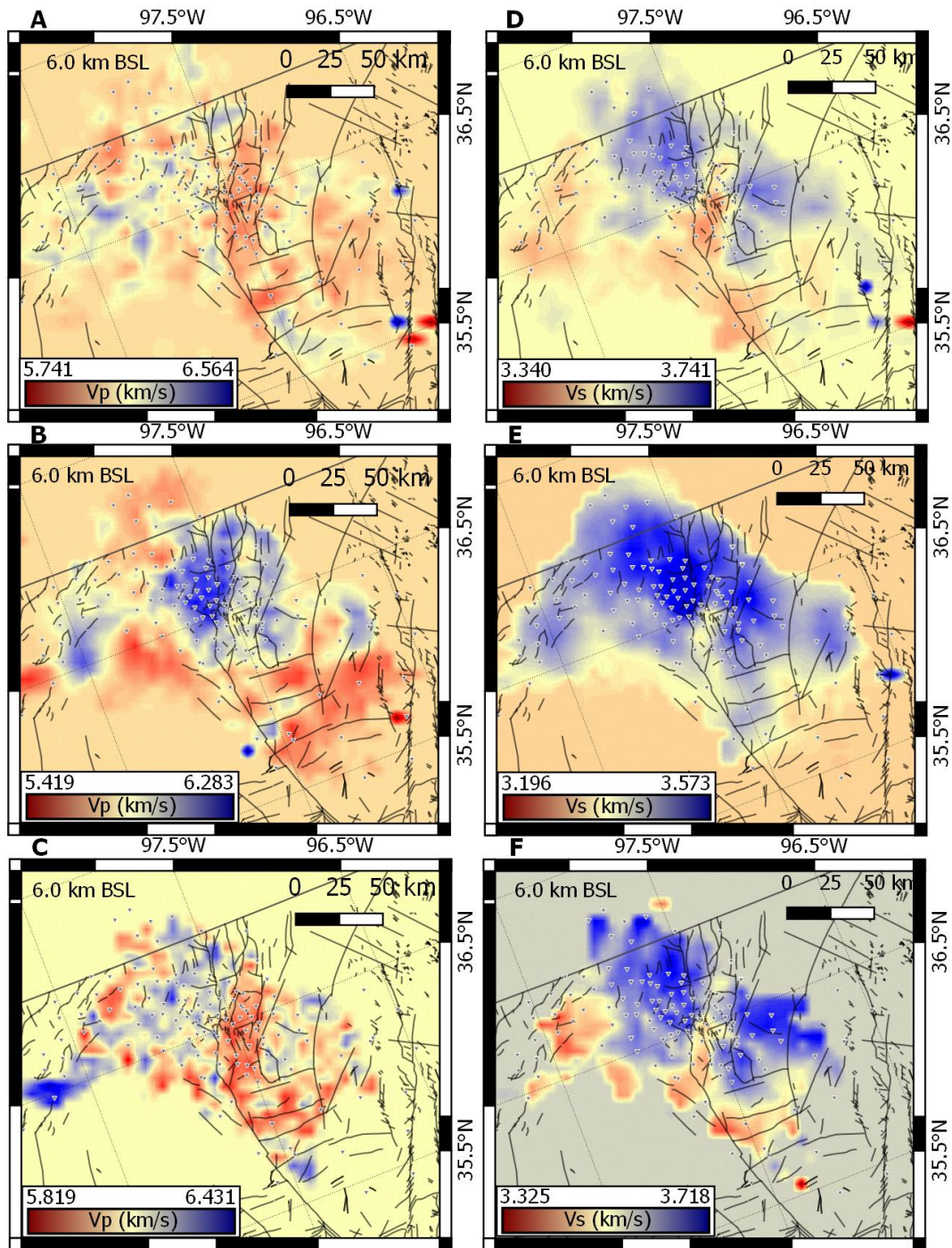


Figure 2.4: Comparison of V_p structure results at the 6 km depth slice for inversions with initial velocity models with (A) 5% faster and (B) 5% slower seismic velocities compared to the model implemented in Chapter 1 (Figure 1.3.A). Results are also shown for (C) an alternative input earthquake catalog with increased event density (8629 events) and the velocity model from Figure 1.3.A. V_s structure recovery for these simulations are shown in (D), (E), and (F), respectively. Station locations shown as triangles, faults from Marsh & Holland (2016).

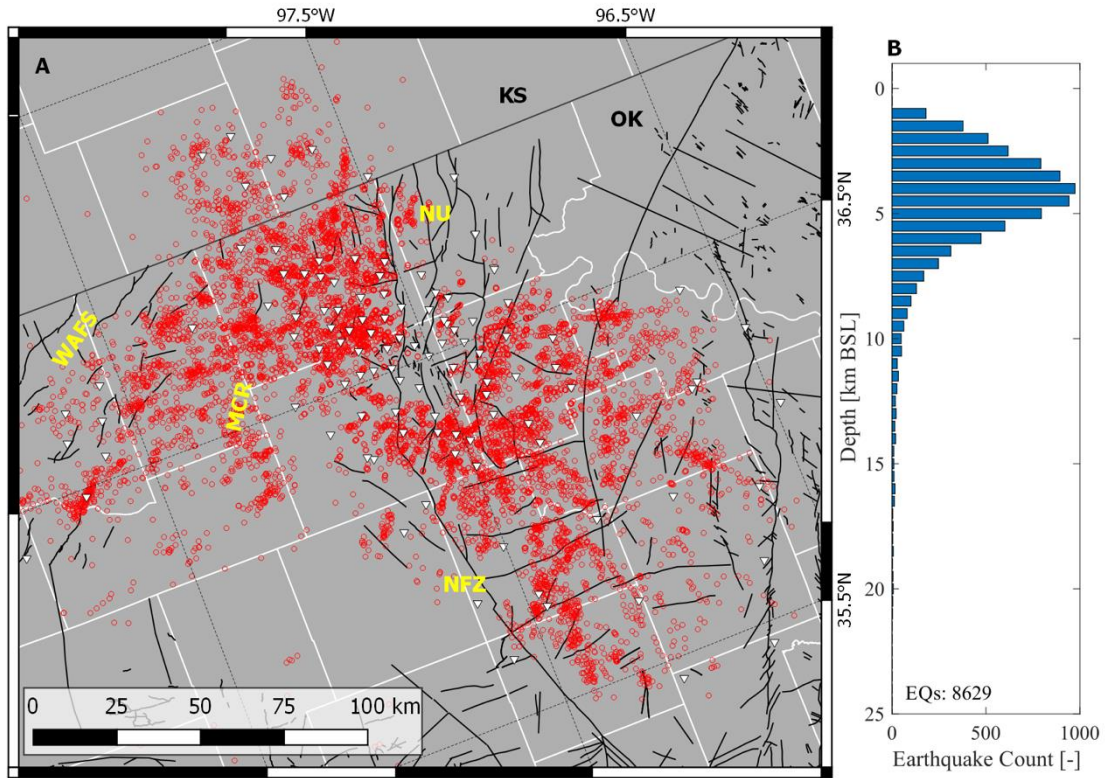


Figure 2.5: Dense (8629) earthquake sub-catalog used for inversion results presented in Figure 2.4 (C & F). (A) epicentral locations (red circles) and station locations (triangles). (B) Depth distribution of sub-catalog earthquakes. Faults, features, and political boundaries match Figure 1.1.

Checkerboard recovery test: 2 node by 2 node anomaly recovery

Checkerboard recovery tests conducted for spatially smaller imposed velocity anomalies were examined to test the limits of velocity structure resolution. Inversion results using synthetic data from an imposed 3-D checkerboard structure with 2 node by 2 node (10 km x 10 km) anomalies consisting of $\pm 3\%$ velocity perturbations are presented for V_p (Figures 2.6 and 2.7) and V_s (Figures 2.8 and 2.9) structure. The imposed checkerboard structure was layered identically to the test in Chapter 1 (Figure 1.6.C). At seismogenic depths (3-8 km BSL; Figure 2.6) V_p anomaly sign and structure are recovered for $pDWS > 150$, but the amplitude of anomalies recovered rarely exceed 60% of the initial imposed anomaly. Recovered V_p structure below 8 km BSL systematically degrades in a similar manner to results presented in Chapter 1 (compare Figures 1.9 and 2.7). V_s anomaly structure is recovered for $sDWS > 150$ at seismogenic depths (3-8 km BSL, Figure 2.8) but anomaly amplitudes rarely exceed 30% of the initial imposed anomalies. Recovered V_s structure below 8 km BSL systematically degrades in a similar manner to results presented in Chapter 1 (compare Figures 1.10 and 2.9).

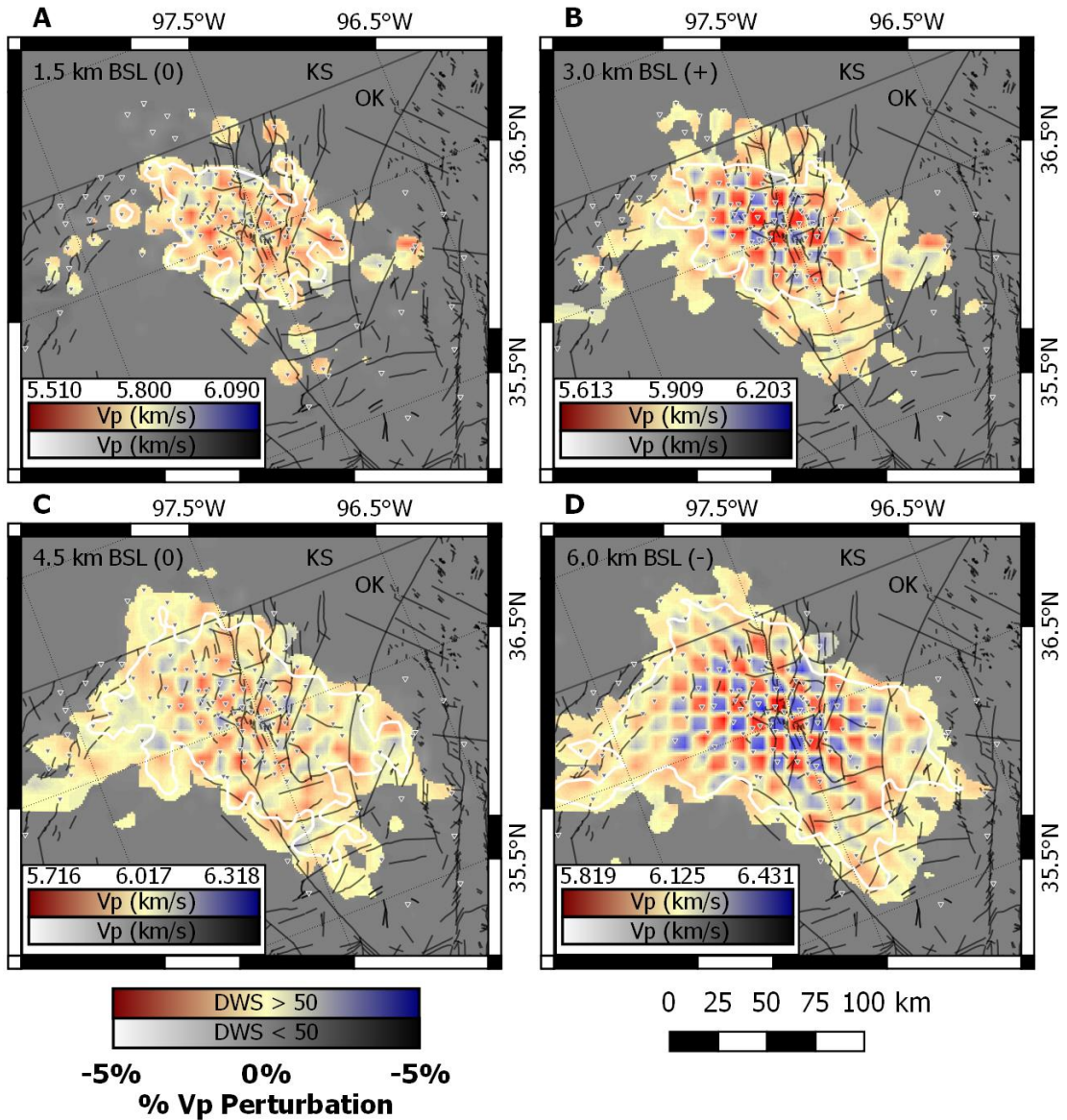


Figure 2.6: Checkerboard test results for V_p structure for 10 km x 10 km checkers (2 node x 2 node) at (A) 1.5 km, (B) 3.0 km, (C) 4.5 km, and (D) 6.0 km. The transition from grayscale to colored results represents the $DWS = 50$ threshold and the white contour is the $DWS = 150$ threshold. Station locations shown as triangles, faults from Marsh & Holland (2016).

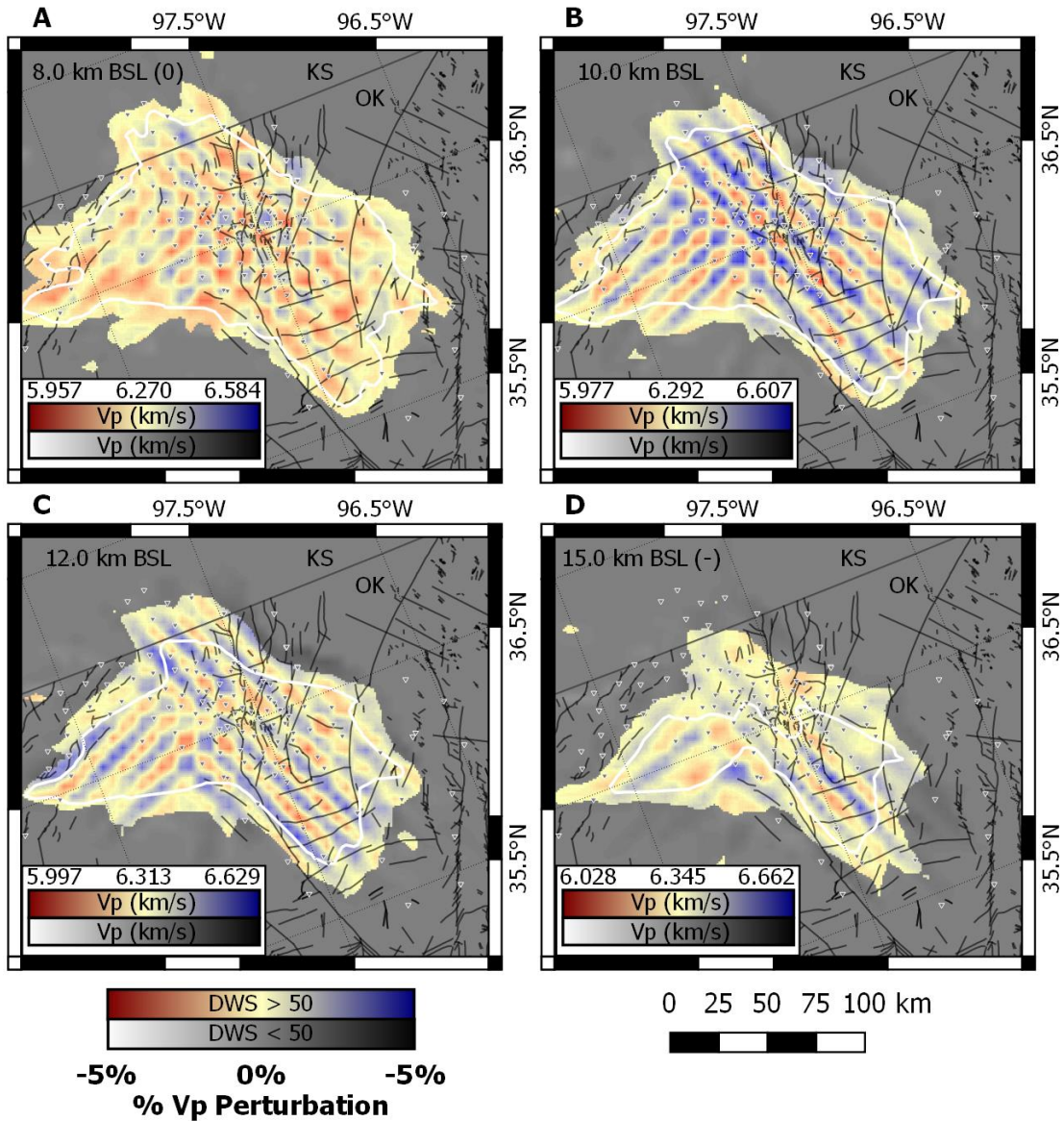


Figure 2.7: Checkerboard test results for V_p structure for 10 km x 10 km checkers (2 node x 2 node) at (A) 8.0 km, (B) 10.0 km, (C) 12.0 km, and (D) 15.0 km. The transition from grayscale to colored results represents the $DWS = 50$ threshold and the white contour is the $DWS = 150$ threshold. Station locations shown as triangles, faults from Marsh & Holland (2016).

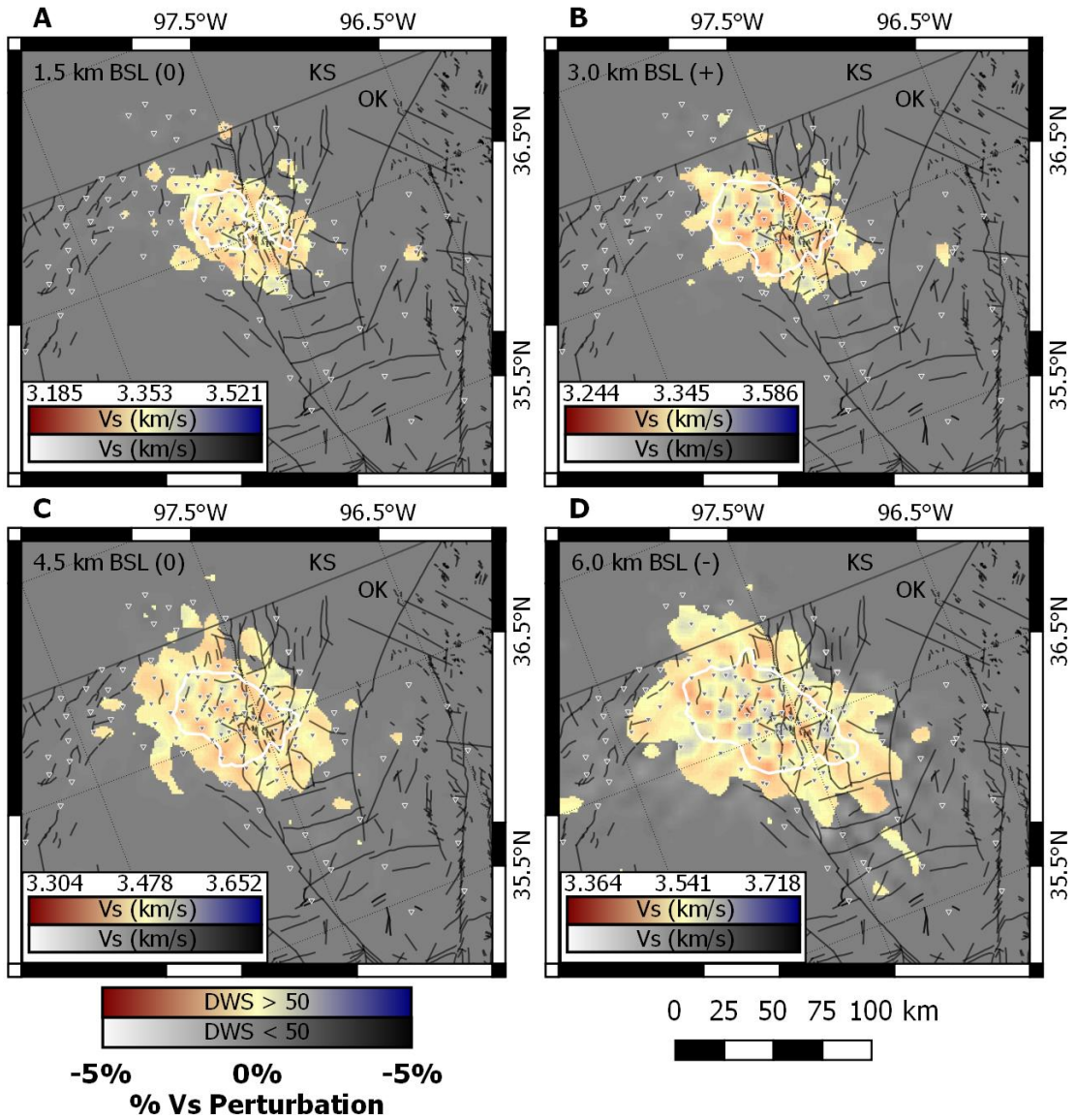


Figure 2.8: Checkerboard test results for V_s structure for 10 km x 10 km checkers (2 node x 2 node) at (A) 1.5 km, (B) 3.0 km, (C) 4.5 km, and (D) 6.0 km. The transition from grayscale to colored results represents the $DWS = 50$ threshold and the white contour is the $DWS = 150$ threshold. Station locations shown as triangles, faults from Marsh & Holland (2016).

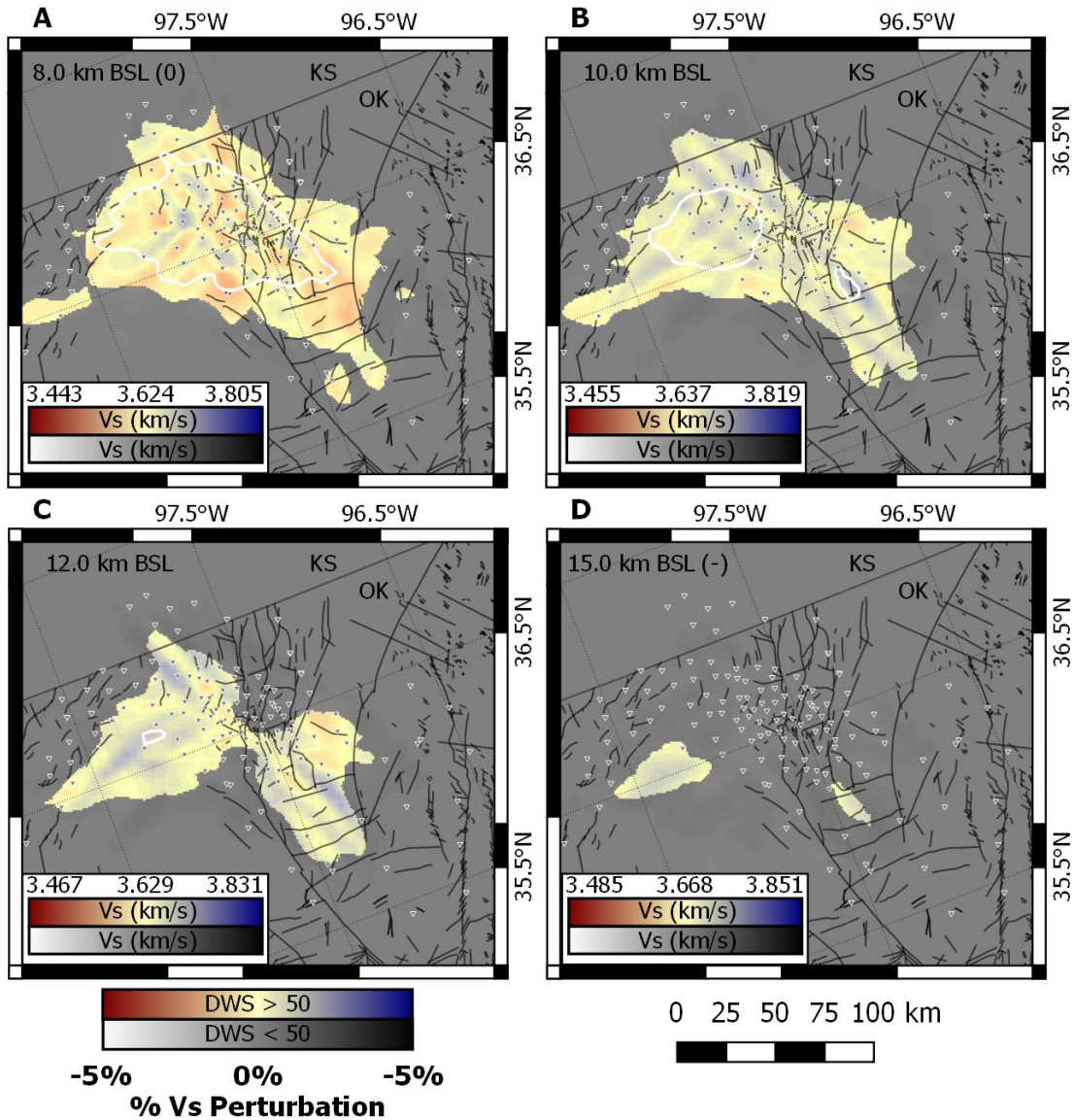


Figure 2.9: Checkerboard test results for V_s structure for 10 km x 10 km checkers (2 node x 2 node) at (A) 8.0 km, (B) 10.0 km, (C) 12.0 km, and (D) 15.0 km. The transition from grayscale to colored results represents the $DWS = 50$ threshold and the white contour is the $DWS = 150$ threshold. Station locations shown as triangles, faults from Marsh & Holland (2016).

REFERENCES

- Darold, A. P., Holland, A. A., Jennifer, K., & Gibson, A. R. (2015). Oklahoma Earthquake Summary Report 2014. *Oklahoma Geological Survey Open File Report, OF1-2015*, 1–46. Retrieved from http://ogs.ou.edu/pubsscanned/openfile/OF1_2015.pdf
- Marsh, S., & Holland, A. (2016). Comprehensive Fault Database and Interpretive Fault Map of Oklahoma. *Oklahoma Geological Survey Open File Report OF2-2016*.

APPENDICES

Appendix A: Earthquake Catalog Development Files:

This appendix documents the data availability and sampling rates for the 131 seismic stations in this study (Table 2.1) and the parameter files used with the Antelope scripts *dbdetect*, *ttgrid*, and *dbgrassoc* to develop initial earthquake catalogs from waveform data (Tables 2.2, 2.3, 2.4, and 2.5).

Table 2.1: Station Sampling Rates (2013-2017). Blank entries indicate no change in station sampling rate (SR) for the duration of the data used in this study.

<i>Station</i>	<i>Net</i>	SR1		SR2		SR3				Off Date		
		<i>sps</i>	<i>ON Year</i>	<i>On DOY</i>	<i>sps</i>	<i>ON Year</i>	<i>On DOY</i>	<i>sps</i>	<i>ON Year</i>	<i>On DOY</i>	<i>Year</i>	<i>DOY</i>
<i>KNG1</i>	ZD	100	2015	91							2015	365
<i>ALF1</i>	XR	200	2016	90	100	2016	323	200	2017	77	2017	150
<i>ALL1</i>	XR	200	2016	85	100	2016	322	200	2017	82	2017	152
<i>BCO1</i>	XR	200	2016	86	100	2016	322	200	2016	353	2017	144
<i>BCO2</i>	XR	200	2016	88	100	2016	319	200	2017	78	2017	145
<i>BCOK</i>	XR	200	2016	91	100	2015	91	200	2016	355	2017	152
<i>BER1</i>	XR	100	2016	321							2017	88
<i>BLA1</i>	XR	200	2016	89	100	2016	322	200	2017	44	2017	148
<i>BRY1</i>	XR	200	2016	89	100	2016	324	200	2017	86	2017	144
<i>BUF1</i>	XR	200	2016	84	100	2016	320	200	2017	65	2017	139
<i>BUF2</i>	XR	200	2016	91	100	2016	320	200	2017	66	2017	143
<i>CAP1</i>	XR	200	2017	96							2017	153
<i>CAR1</i>	XR	200	2016	77	100	2016	323	200	2017	78	2017	144
<i>CRE2</i>	XR	200	2017	98							2017	146
<i>DIR1</i>	XR	200	2016	90	100	2016	320	200	2017	86	2017	98
<i>ENI1</i>	XR	200	2016	201	100	2016	323	200	2017	69	2017	140
<i>FGO1</i>	XR	200	2016	57							2016	190
<i>FGO2</i>	XR	200	2016	56							2016	185
<i>FGO3</i>	XR	200	2016	57							2016	192
<i>FGO4</i>	XR	200	2016	58							2016	197
<i>GLE1</i>	XR	200	2016	83	100	2016	319	200	2017	72	2016	313
<i>GRA1</i>	XR	200	2016	200	100	2016	320	200	2017	84	2016	320
<i>HAC1</i>	XR	200	2016	203	100	2016	322	200	2017	84	2016	322
<i>KRE1</i>	XR	200	2016	90	100	2016	324	200	2017	86	2017	147
<i>LIB1</i>	XR	200	2016	85	100	2016	324	200	2017	86	2017	144
<i>LIB2</i>	XR	200	2016	86	100	2016	324	200	2017	78	2017	148
<i>MAR1</i>	XR	200	2016	93	100	2016	321	200	2017	80	2016	321
<i>MED1</i>	XR	200	2016	92							2016	249

<i>MED2</i>	XR	200	2016	84	100	2016	320	200	2017	85	2017	150
<i>MIL1</i>	XR	200	2016	91	100	2016	320	200	2016	353	2017	113
<i>MLO1</i>	XR	200	2016	202	100	2016	320	200	2017	84	2017	113
<i>NAS1</i>	XR	250	2017	89							2017	156
<i>NAS2</i>	XR	200	2017	100							2017	152
<i>NOB1</i>	XR	200	2016	91	100	2016	320	200	2017	82	2017	149
<i>NOB2</i>	XR	200	2016	83	100	2016	327	200	2017	85	2017	149
<i>NUM1</i>	XR	200	2016	89	100	2016	325	200	2016	365	2017	145
<i>OAK1</i>	XR	200	2016	85	100	2016	322	200	2017	146	2016	325
<i>OLI1</i>	XR	200	2016	84	100	2016	321	200	2017	61	2017	146
<i>OWE1</i>	XR	200	2016	86	100	2016	323	200	2016	324	2017	138
<i>OWE2</i>	XR	200	2016	83	100	2016	320	200	2017	61	2017	138
<i>OWE3</i>	XR	200	2016	83	100	2016	323	200	2017	84	2017	98
<i>PER1</i>	XR	200	2016	204	100	2016	321	200	2017	87	2017	148
<i>REN1</i>	XR	200	2016	88	100	2016	324	200	2017	84	2016	324
<i>REN2</i>	XR	200	2016	90	100	2016	324	200	2017	84	2017	145
<i>RI01</i>	XR	200	2016	91	100	2016	324	200	2017	98	2017	150
<i>RRO1</i>	XR	200	2016	83	100	2016	321	200	2017	74	2017	145
<i>RTA1</i>	XR	200	2017	96							2017	153
<i>SF01</i>	XR	200	2016	82	100	2016	324	200	2017	86	2017	147
<i>SF02</i>	XR	200	2016	87	100	2016	323	200	2017	73	2017	142
<i>SF03</i>	XR	200	2016	90	100	2016	327	200	2017	85	2017	150
<i>VAL1</i>	XR	200	2016	88							2016	249
<i>WAL1</i>	XR	200	2017	99							2017	153
<i>WKT1</i>	XR	200	2017	97							2017	154
<i>WOO1</i>	XR	200	2014	262	100	2016	322	200	2016	324	2016	298
<i>WOO2</i>	XR	200	2016	84	100	2016	321	200	2017	93	2017	145
<i>WRO1</i>	XR	200	2016	83	100	2016	322	200	2017	87	2017	145
<i>WRO2</i>	XR	200	2016	92	100	2016	321	200	2017	87	2017	146
<i>WV01</i>	XR	200	2016	93	100	2016	321	200	2017	7	2017	149
<i>A005</i>	SU	100	2015	91							2016	184
<i>A008</i>	SU	100	2015	91							2016	86
<i>A011</i>	SU	100	2015	95							2016	97
<i>BLOK</i>	OK	100	2015	156							2017	190
<i>CROK</i>	OK	100	2015	91							2017	190
<i>GC02</i>	OK	100	2015	91							2017	190
<i>GORE</i>	OK	200	2015	156							2017	190
<i>QUOK</i>	OK	100	2015	91							2017	190
<i>U32A</i>	OK	100	2016	5							2017	190
<i>STN01</i>	NX	100	2013	99							2016	91
<i>STN02</i>	NX	100	2013	98							2016	91
<i>STN03</i>	NX	100	2013	134							2016	91

STN04	NX	100	2013	132						2016	91
STN05	NX	100	2013	128						2016	91
STN06	NX	100	2013	128						2016	91
STN07	NX	100	2013	97						2016	91
STN08	NX	100	2013	126						2016	91
STN09	NX	100	2013	97						2016	91
STN10	NX	100	2013	125						2016	91
STN11	NX	100	2013	129						2016	91
STN12	NX	100	2013	125						2016	91
STN13	NX	100	2013	132						2016	91
STN14	NX	100	2013	97						2016	91
STN15	NX	100	2013	97						2016	91
STN16	NX	100	2013	126						2016	91
STN17	NX	100	2013	125						2016	91
STN18	NX	100	2013	130						2016	91
STN19	NX	100	2013	152						2016	91
STN20	NX	100	2013	151						2016	91
STN21	NX	100	2013	153						2016	91
STN22	NX	100	2013	151						2016	91
STN23	NX	100	2013	154						2016	91
STN24	NX	100	2013	153						2016	91
STN26	NX	100	2013	156						2016	91
STN31	NX	100	2013	134						2016	91
STN32	NX	100	2013	149						2016	91
STN33	NX	100	2013	135						2016	91
STN34	NX	100	2013	134						2016	91
STN35	NX	100	2013	135						2016	91
KAY1	NQ	200	2015	91						2015	147
KAN01	GS	200	2017	86						2017	197
KAN05	GS	200	2017	86						2017	197
KAN06	GS	200	2017	86						2017	197
KAN08	GS	200	2017	86						2017	197
KAN09	GS	200	2017	86						2017	197
KAN13	GS	200	2015	90						2017	190
KAN14	GS	200	2015	91						2017	190
KAN17	GS	200	2017	86						2017	197
OK029	GS	200	2016	356						2017	190
OK032	GS	200	2016	357						2017	84
OK035	GS	200	2016	358						2017	75
OK038	GS	100	2017	86						2017	197
OK916	GS	200	2015	361						2016	269
BLT1	CU	250	2017	92						2017	153

<i>BRP1</i>	CU	250	2017	89							2017	154
<i>CAP2</i>	CU	250	2017	99							2017	156
<i>CRE1</i>	CU	250	2017	94							2017	156
<i>EA01</i>	CU	250	2015	90							2016	326
<i>EA02</i>	CU	250	2015	90							2016	326
<i>EA03</i>	CU	250	2015	90							2016	326
<i>EA04</i>	CU	250	2015	88							2016	326
<i>EA05</i>	CU	250	2015	91							2016	326
<i>EA06</i>	CU	250	2015	90							2016	326
<i>EA07</i>	CU	250	2015	90							2015	210
<i>EA08</i>	CU	250	2015	89							2016	229
<i>EA09</i>	CU	250	2015	89							2016	266
<i>EA10</i>	CU	250	2015	88							2016	326
<i>EA11</i>	CU	250	2015	210							2016	326
<i>GOL1</i>	CU	250	2017	92							2017	156
<i>HAW1</i>	CU	250	2017	89							2017	154
<i>HD01</i>	CU	250	2017	92							2017	153
<i>MAN1</i>	CU	250	2017	95							2017	156
<i>MAN2</i>	CU	200	2017	96							2017	153

Table 2.2: *dbdetect.PphaseBCEH.pf*. This parameter file is used as an input to the *dbdetect* Antelope script to detect P phase arrivals on the vertically-oriented (Z-channel) seismometer channels using a short-term-average / long-term-average detection trigger.

```

#   Parameter file for orbdetect
#   Following are required and are used as overall defaults

ave_type    rms    # Method for averaging (rms or filter)
sta_twin    0.2    # short term average time window
sta_tmin    0.2    # short term average minimum time for average
sta_maxtgap 0.5    # short term average maximum time gap
lta_twin    1.0    # long term average time window
lta_tmin    0.5    # long term average minimum time for average
lta_maxtgap 1.0    # long term average maximum time gap
nodet_twin  0.0    # no detection if on time is less than this
pamp        500.0  # plot amplitude
thresh      3.0    # detection SNR threshold
threshoff   1.7    # detection-off SNR threshold
det_tmin    0.02   # detection minimum on time
det_tmax    0.5    # detection maximum on time
h           0      # plot channel height in pixels
filter      BW 1.0 4 50.0 0 # default filter
iphase      D      # default iphase for detections

process_twin 60.0  # data is processed in hunks of this duration
onset_search_offset -1.0 #time offset in front of detection to look for onset

#   At least one default band must be set set up in the bands table
#   parameter values override default values above for each band

bands &Tbl{
    &Arr{
        sta_twin    0.2
        sta_tmin    0.2
        sta_maxtgap 0.5
        lta_twin    1.0
        lta_tmin    0.5
        lta_maxtgap 1.0
        pamp        500.0
        filter      BW 1.0 4 50.0 0
    }
}

#   At least one data channel must be specified in the stachans table

stachans    &Tbl{
#   sta    chan
.* [BCHE][HN]Z...

```

```
}  
  
# station/channels to reject  
  
reject &Tbl{  
# sta chan  
}
```

Table 2.3: *dbdetect.SphaseBCEH.pf*. This parameter file is used as an input to the *dbdetect* Antelope script to detect S phase arrivals on the north-oriented (N-channel or 1-channel, depending on array operator) seismometer channels using a short-term-average / long-term-average detection trigger.

```

#   Parameter file for orbdetect
#   S phase detection for EnidArray
#   Following are required and are used as overall defaults

ave_type    rms    # Method for averaging (rms or filter)
sta_twin    0.2    # short term average time window
sta_tmin    0.2    # short term average minimum time for average
sta_maxtgap 0.5    # short term average maximum time gap
lta_twin    2      # long term average time window
lta_tmin    1      # long term average minimum time for average
lta_maxtgap 1.0    # long term average maximum time gap
nodet_twin  0.1    # no detection if on time is less than this
pamp        500.0  # plot amplitude
thresh      4      # detection SNR threshold
threshoff   2      # detection-off SNR threshold
det_tmin    0.02   # detection minimum on time
det_tmax    0.5    # detection maximum on time
h           0      # plot channel height in pixels
filter      BW 0.1 4 5.0 0 # default filter
iphase      D      # default iphase for detections

process_twin 60.0  # data is processed in hunks of this duration
onset_search_offset -1.0 # time offset in front of detection to look for onset

#   At least one default band must be set set up in the bands table
#   parameter values override default values above for each band

bands &Tbl{
  &Arr{
    sta_twin    0.2
    sta_tmin    0.2
    sta_maxtgap 0.5
    lta_twin    2
    lta_tmin    1
    lta_maxtgap 1.0
    pamp        500.0
    filter      BW 0.1 4 5.0 0
  }
}

#   At least one data channel must be specified in the stachans table

stachans    &Tbl{

#   sta   chan

```

```

.* [BCHE][HN][N1]...
}
# station/channels to reject

reject &Tbl{
# sta chan
BCOK HHN
}

# Individual netstachan parameters may be overridden below - following
# entries are optional
[EA07][CROK]/HHN &Arr{
bands &Tbl{
&Arr{
sta_twin 0.2
sta_tmin 0.2
sta_maxtgap 0.5
lta_twin 2.0
lta_tmin 1.0
lta_maxtgap 1.0
pamp 500.0
filter BW 1.0 4 5.0 0
}
# &Arr{
# sta_twin 2.0
# sta_tmin 2.0
# sta_maxtgap 0.5
# lta_twin 20.0
# lta_tmin 10.0
# lta_maxtgap 4.0
# pamp 500.0
# filter BW 0.8 4 3.0 4
#
# &Arr{
# sta_twin 1.0
# sta_tmin 1.0
# sta_maxtgap 0.5
# lta_twin 10.0
# lta_tmin 5.0
# lta_maxtgap 4.0
# pamp 500.0
# filter BW 3.0 4 0 0
#
# }
}
h 50
}

```

Table 2.4: *ttgridnts.pf*. This parameter file is used with the *ttgrid* Antelope script to create a travel-time look-up-table used in phase association and event location via grid-search (*dbgrassoc*, parameter file in Table 2.5). The *geoff2* model is identical to the velocity used by Lambert (2017).

```
# parameter file for ttgrid
grids &Arr{
  local &Arr{
    mode      edp # defines an equal-distance projection regular 3-D mesh
    latr      36.5 # reference latitude (origin of grid)
    lonr      -97.5 # reference longitude (origin of grid)
    nx        100 # Number of X-axis distance grid nodes
    ny        100 # Number of Y-axis distance grid nodes
    xmin      -1.5 # Minimum value of X-axis distance grid in degrees
    xmax      1.5 # Maximum value of X-axis distance grid in degrees
    ymin      -1.5 # Minimum value of Y-axis distance grid in degrees
    ymax      1.5 # Maximum value of Y-axis distance grid in degrees
    strike    90.0 # Angle from north clockwise in degrees to the X-axis
    compute_P yes # yes = Compute P travel times
    compute_S yes # yes = Compute S travel times
    method    tt1dcvl # method for computing travel times
    model     geoff2 # model for computing travel times
    depths &Tbl{
      0.0
      0.5
      1.0
      1.5
      2.0
      3.0
      4.0
      5.0
      6.0
      8.0
      10.0
      12.0
      14.0
      16.0
      20.0
      24.0
      32.0
      41.0
      56.0
      70.0
      80.0
      100.0
      140.0
    }
  }
}
```

Table 2.5: *dbgrassoc.test1.pf*. This parameter file was used with the *dbgrassoc Antelope* script to associate detected phase arrivals (see text, Tables 2.2 & 2.3) and estimate hypocentral parameters (i.e., location, depth, and origin time) them within a travel time grid (see text, Table 2.4) using a grid-search method to minimize travel time residuals.

```
# Parameter file for dbgrassoc

process_time_window 60      # Main detection processing time window
process_ncycle      0      # how often to do detection processing, in detections
process_tcycle      5      # how often to do detection processing, in delta time
trigger_number_stations 6    #number of stations for trigger initiation
trigger_time_window 25      # time window in seconds for trigger initiation

grid_params &Arr{
  local &Arr{
    nsta_thresh 8    # Minimum allowable number of stations
    nxd          11  # Number of east-west grid nodes for depth scans
    nyd          11  # Number of north-south grid nodes for depth scans
    cluster_twin 1.5 # Clustering time window
    try_S        yes # yes = Try observations as both P and S
                  # no = Observations are P only
    associate_S  yes # yes = Try to associate observations as both P and S
    reprocess_S no   # yes = Reprocess when new S-associations found
    # phase_sifter 1
    drop_if_on_edge yes #Drop is a solution is on the edge of the grid
    P_channel_sifter ..[Z] #Only associate P picks with ..Z channels
    S_channel_sifter ..[NE12] #Only associate S picks with ..[NE]
  }
}

channels
  auth          dbgrassoc
  nondefining_association_P_maxresid 0.4 #maximum residual for non-
defining P arrival associations
  nondefining_association_S_maxresid 0.4 #maximum residual for non-
defining S arrival associations
  priority      5
  use_dwt       no
  dwt_dist_near 0.02
  dwt_wt_near   1.0
  dwt_dist_far  0.08
  dwt_wt_far    0.0
  use_dwts      yes
  dwts_dist_near 0.02
  dwts_wt_near  1.0
  dwts_dist_far 0.08
  dwts_wt_far   0.0
```

```

    }
}

# parameters for "smart" association

assoc_method      tt1dcv1 # method for computing predicted travel times
assoc_model       geoff2 # velocity model for computing predicted travel times
assoc_phases      basic # phase list for computing predicted travel times (see tt(3))
assoc_P_thresh    0.2   # P-residual threshold for associations
assoc_S_thresh    0.2   # S-residual threshold for associations
assoc_ignoreiphs no    # should the arrival row iphase value be ignored?
assoc_firstphase  yes   # should only the earliest predicted phase be used?

assoc_screen_new   time
assoc_screen_old   (time-360.0)::(time+360.0)
                  # these are screening database expressions that should
                  # match the existing (old) origins with the new origin for
                  # association processing
assoc_expression   $nass>=$nars
                  # this is a database expression that should evaluate
                  # to true whenever an association is valid

author_priority &Arr{ # prefpr priority as a function of assoc author
}

```

Appendix B: TomoDD Solution Control Files

This appendix contains the solution control files used for relocation of the initial earthquake catalogs developed in Antelope (Table 2.6) and the solution control file for the best fit inversion discussed in this study (Table 2.7).

Table 2.6: tomoDD.inp – This TomoDD solution control file instructs TomoDD to conduct a single relocation-only-inversion to relocate the input earthquake catalog. After Zhang & Thurber (2003, 2006)

```
*--- input file selection
* cross correlation diff times:
../0.Common_Inputs/dt.cc.empty
*
*catalog P diff times:
../0.Common_Inputs/dt.ct
* catalog absolute times
../0.Common_Inputs/absolute.PandS.dat
*
* event file:
../0.Common_Inputs/event.tomo.sel
*
* station file:
../0.Common_Inputs/station.m.sel
*
*--- output file selection
* original locations:
./test.loc
* relocations:
./test.reloc
* station information:
./test.sta
* residual information:
./test.res
* source paramater information:
* PS_EQCAT10579_5x5x1.src

*Output velocity
./test.vel
* Vp model
Vp_model.dat
* Vs model
Vs_model.dat
*--- data type selection:
* IDAT: 0 = synthetics; 1= cross corr; 2= catalog; 3= cross & cat
* IPHA: 1= P; 2= S; 3= P&S
* DIST:max dist [km] between cluster centroid and station
* IDAT IPHA DIST
  2  3  100.0
```

```

*
*--- event clustering:
* OBSCC:  min # of obs/pair for crosstime data (0= no clustering)
* OBSCT:  min # of obs/pair for network data (0= no clustering)
* CC_format Cross Correlation data format (1 = hypoDD form, 2 = tomoDD form)
* OBSCC OBSCT CC_format
  0  0  1
*
*--- solution control:
* ISTART:    1 = from single source; 2 = from network sources
* ISOLV:     1 = SVD, 2=lsqr
* NSET:      number of sets of iteration with specifications following
* ISTART ISOLV NSET weight1 weight2 weight3 air_depth
  2  2  1  50  50  10  -0.5
* i3D delt1 ndip iskip scale1 scale2 iuses
  3  0  9  1  0.5  1.00  2
* xfac tlim  nitpb(1) nitpb(2) stepl
  1.3  0.002  50  50  0.2
* lat_Orig lon_Orig Z_Orig iorig rota
  36.427 -097.603  0  1  21
*
*--- data weighting and re-weighting:
* NITER:      last iteration to used the following weights
* WTCCP, WTCCS:  weight cross P, S
* WTCTP, WTCTS:  weight catalog P, S
* WRCC, WRCT:    residual threshold in sec for cross, catalog data
* WDCC, WDCT:    max dist [km] between cross, catalog linked pairs
* WTCD:  relative weighting between absolute and differential data
* THRES:  Scalar used to determine the DWS threshold values
* DAMP:    damping (for lsqr only)
*  --- CROSS DATA -----CATALOG DATA ----
* NITER WTCCP WTCCS WRCC WDCC WTCTP WTCTS WRCT WDCT WTCD DAMP
JOINT THRES
  1  0.01  0.01  -9  -9  1.0  0.7  0.7  20  10  100  0  0.2
*--- event selection:
* CID:  cluster to be relocated (0 = all)
* ID:   cuspsids of event to be relocated (8 per line)
* CID
  0
* ID

```

Table 2.7: tomoDD.inp – This TomoDD solution control file instructs TomoDD to conduct the best-fit inversion from Chapter 1 and from Figure 2.4 for a given input dataset and initial velocity model. After Zhang & Thurber (2003, 2006).

```

*--- input file selection
* cross correlation diff times:
../0.1.Common_Inputs/dt.cc.empty
*
*catalog P diff times:
../0.1.Common_Inputs/dt.ct
* catalog absolute times
../0.1.Common_Inputs/absolute.dat
*
* event file:
../0.1.Common_Inputs/event.eq.sel
*
* station file:
../0.1.Common_Inputs/station.m.all.dat
*
*--- output file selection
* original locations:
./test.loc
* relocations:
./test.reloc
* station information:
./test.sta
* residual information:
./test.res
* source parameter information:
* PS_EQCAT10579_5x5x1.src

*Output velocity
./test.vel
* Vp model
Vp_model.dat
* Vs model
Vs_model.dat
*--- data type selection:
* IDAT: 0 = synthetics; 1= cross corr; 2= catalog; 3= cross & cat
* IPHA: 1= P; 2= S; 3= P&S
* DIST:max dist [km] between cluster centroid and station
* IDAT IPHA DIST
  2  3  100.0
*
*--- event clustering:
* OBSCC: min # of obs/pair for crosstime data (0= no clustering)
* OBSCT: min # of obs/pair for network data (0= no clustering)
* CC_format Cross Correlation data format (1 = hypoDD form, 2 = tomoDD form)
* OBSCC OBSCT CC_format

```

```

0 0 1
*
*--- solution control:
* ISTART:      1 = from single source; 2 = from network sources
* ISOLV:       1 = SVD, 2=lsqr
* NSET:        number of sets of iteration with specifications following
* ISTART ISOLV NSET weight1 weight2 weight3 air_depth
  2  2  9  15  15  10  -0.3
* i3D delt1 ndip iskip scale1 scale2 iuses
  3  0  9  1  0.5  1.00  2
* xfac tlim nitpb(1) nitpb(2) stepl
  1.3 0.002 50 50 0.2
* lat_Orig lon_Orig Z_Orig iorig rota
  36.427 -097.603 0 1 21
*
*--- data weighting and re-weighting:
* NITER:                last iteration to used the following weights
* WTCCP, WTCCS:         weight cross P, S
* WTCTP, WTCTS:         weight catalog P, S
* WRCC, WRCT:           residual threshold in sec for cross, catalog data
* WDCC, WDCT:           max dist [km] between cross, catalog linked pairs
* WTCD: relative weighting between absolute and differential data
* THRES: Scalar used to determine the DWS threshold values
* DAMP:                 damping (for lsqr only)
* --- CROSS DATA ----- CATALOG DATA ----
* NITER WTCCP WTCCS WRCC WDCC WTCTP WTCTS WRCT WDCT WTCD DAMP
JOINT THRES
1 0.01 0.01 -9 -9 0.1 0.08 9 10 10 75 0 0.2
1 0.01 0.01 -9 -9 0.1 0.08 8 10 10 200 1 0.2
1 0.01 0.01 -9 -9 0.1 0.08 8 8 10 75 0 0.2
1 0.01 0.01 -9 -9 0.1 0.08 7 8 10 200 1 0.2
1 0.01 0.01 -9 -9 0.1 0.08 7 7 10 75 0 0.2
1 0.01 0.01 -9 -9 1.0 0.8 7 7 1 200 1 0.2
1 0.01 0.01 -9 -9 1.0 0.8 7 5 1 75 0 0.2
1 0.01 0.01 -9 -9 1.0 0.8 6 5 1 200 1 0.2
1 0.01 0.01 -9 -9 1.0 0.8 6 3 1 75 0 0.2
*
*--- event selection:
* CID: cluster to be relocated (0 = all)
* ID: cusps of event to be relocated (8 per line)
* CID
  0
* ID

```

Appendix C: Best Fit Inversion Directory & Initialization Instructions

This appendix details the directory structure, files, and command needed to initialize a realization of the best-fit TomoDD inversion presented in this study.

All files needed for running a version of the best-fit inversion presented in this thesis are contained in:

/ld4/OK_Gap/OK_Gap_NTS/Stevens_etal_2018_TomoDD/BestFitRun/

A *.zip archive of the BestFitRun/ directory is included as a supplementary file to this thesis: Stevens_CU_Thesis_BestFitModel.zip

This directory contains two sub-directories:

0.1.Common_Inputs/

This directory contains input data files including initial event locations (event.eq.sel), absolute travel time data (absolute.dat), and catalog differential travel time data (dt.ct). The directory also contains a file to contain cross-correlation differential times, but these were not implemented in this study so there is a placeholder file (dt.cc.empty).

These files are purposely kept separate from the folder containing the inversion realizations to save hard-drive space. This is particularly useful for when conducting large suites of parametric tests that are all based on the same input database, but variable solution control parameterizations.

0.2.Inversion_Run/

This directory contains the initial velocity model file (MOD) and the inversion solution control file (tomoDD.inp) needed to run a TomoDD inversion. The tomoDD.inp file points to shared input data in the 0.1.Common_Inputs directory and reads in these data upon initialization of TomoDD10. All input file locations are written as relative paths that operate in the sub-directory structure starting from a common directory (*BestFitRun/ in this case). The MOD file must be located in the same directory as tomoDD.inp.

The directory also contains output files from a successful TomoDD simulation using the files as-is, including velocity structure depth-slice results that were interpolated to 1 km x 1 km grid spacings using a trilinear interpolation scheme, consistent with methods from Zhang & Thurber (2003, 2006).

Initialization of a TomoDD run is accomplished by invoking:

```
tomoDD10 >& tdd.out
```

when in the 0.2.Inversion_Run/ sub-directory. The muted pipe (>&) to an output file is optional, but recommended.

The FORTRAN source code scripts for TomoDD used in this study are located in:
/ld4/OK_Gap/OK_Gap_NTS/TomoDD/TomoDD10/

Appendix D: Project Data Map

This appendix details the directory structure that houses data, parameter files, scripts, and model realizations used in this study. All files are located on the Kone server operated by the Department of Earth and Atmospheric Sciences at Cornell University.

Initial Earthquake Catalogs – Antelope databases with which detection, association and grid-search location of earthquakes were conducted with Antelope scripts and parameter files detailed in Appendix A. Databases “reassoc_reloc” and “nanodb” were developed by Lambert (2017).

XR Network Antelope Database (2016-2017 Data):
/ld4/OK_Gap/OK_Gap_NTS/DB_MERGE_3/dbokmerge
CU Network Antelope Database (2015-2016 Data):
/ld2/Oklahoma/Enid_Gap/reassoc_reloc
NX Network Antelope Database (2013-2015 Data):
/ld3/OK_Data/Nano_Data/nanodb

Earthquake Catalog Generation Parameter File (Tables 2.2-2.5) Locations – File paths for parameter files used to develop initial earthquake catalogs. These built upon parameter files used by Lambert (2017).

/ld4/OK_Gap/OK_Gap_NTS/DB_MERGE_3/pf
/dbdetect.PphaseBCEH.pf
/dbdetect.SphaseBCEH.pf
/ttgridnts.pf
/dbgrassoc.test1.pf
Bash Wrapper Script for Moving-Window Phase Detection & Event Location:
/ld4/OK_Gap/OK_Gap_NTS/DB_MERGE_3/scripts/PAD_v1.6.1.sh

Initial Catalog Relocation Results via Single Relocation-Only-Inversion (Figure 1.1) – Event catalogs for each of the antelope databases listed above were relocated independently to expediate the relocation inversion.

/ld4/OK_Gap/OK_Gap_NTS/HypoDD/1P.NXruns/1P.N.1.D15nCXd1.PS.1ITER/test.reloc.001.001
/ld4/OK_Gap/OK_Gap_NTS/HypoDD/2P.CUruns/2P.N.1.D15nCXd1.PS.1ITER/test.reloc.001.001
/ld4/OK_Gap/OK_Gap_NTS/HypoDD/3P.XRruns/3P.N.1.D15nCXd1.PS.1ITER/test.reloc.001.001

Earthquake Sub-Catalog for TomoDD Inversions – Files listed here are the input data files for tomographic inversions presented in this study, with the exception of the dense earthquake sub-catalog (Figures 2.4 & 2.5; see entry below)

Event Locations (Figure 1.4):
/ld4/OK_Gap/OK_Gap_NTS/Stevens_etal_2018_TomoDD/D15B_Param_Runs/0.1.Common_Inputs/event.eq.sel
Phase Travel Time Data:

/ld4/OK_Gap/OK_Gap_NTS/Stevens_etal_2018_TomoDD/D15B_Param_Runs/0.1.
Common_Inputs/absolute.dat
Differential Travel Time Calculation Parameter File:
/ld4/OK_Gap/OK_Gap_NTS/Stevens_etal_2018_TomoDD/D15B_Param_Runs/0.1.
Common_Inputs/ph2dt.ensemble200km.inp
Differential Travel Time Data:
/ld4/OK_Gap/OK_Gap_NTS/Stevens_etal_2018_TomoDD/D15B_Param_Runs/0.1.
Common_Inputs/dt.ct

Double Difference Tomography Source Code

Note: the source-code for TomoDD10 was slightly modified to produce a separate output file for pDWS (pdws.dat) and sDWS (sdws.dat) metrics, as well as predicted travel times (pred.dat). The modified version of this script is in directory:
/ld4/OK_Gap/OK_Gap_NTS/TomoDD/TomoDD10/

Parametric Tests (Figure 1.5) – The 101 model realizations used for parametric testing in this thesis are located at file paths described below. Subdirectory naming convention was based upon key parameters, as described below.

Primary Directory:

/ld4/OK_Gap/OK_Gap_NTS/Stevens_etal_2018_TomoDD/D15B_Param_Runs/

Sub-Directories:

wt15.dXrYj/

or

wt15.dZ/

where

X = [75, 100, 125, 150, 175, 200, 225, 250, 300, 400], representing relocation-only-inversion damping parameterization

Y = [75, 100, 125, 150, 175, 200, 225, 250, 300, 400], representing coupled-inversion damping parameterization

Z = [75, 100, 125, 150, 175, 200, 225, 250, 300, 400], when relocation-only-inversion damping and coupled-inversion damping values are equal

Summary File:

/ld4/OK_Gap/OK_Gap_NTS/Stevens_etal_2018_TomoDD/D15B_Param_Runs/parametric_tests_summary.csv

Checkerboard Recovery Test (Figures 1.6-1.10). The 3 node by 3 node checkerboard recovery test consisted of 3 stages: 1) forward modeling of synthetic travel times, 2) isolation of only extant station-event-phase combinations in the synthetic data and the addition of white noise errors, and 3) inversion of synthetic data using the best-fit inversion parameterization.

Forward Model:

/ld4/OK_Gap/OK_Gap_NTS/Stevens_etal_2018_TomoDD/D15B_Synth_Runs/CX.y3x3zlp3n6p10n15_p3_Ov2z/F.Forward/

Synthetic Data Directory:

/ld4/OK_Gap/OK_Gap_NTS/Stevens_etal_2018_TomoDD/D15B_Synth_Runs/CX.y3x3zlp3n6p10n15_p3_Ov2z/T.Transfer/

Inverse Model Directory:

/ld4/OK_Gap/OK_Gap_NTS/Stevens_etal_2018_TomoDD/D15B_Synth_Runs/CX.y3x3zlp3n6p10n15_p3_Ov2z/I.wt15x10.d75r200j/

Recovered Vp Structure:

/ld4/OK_Gap/OK_Gap_NTS/Stevens_etal_2018_TomoDD/D15B_Synth_Runs/CX.y3x3zlp3n6p10n15_p3_Ov2z/I.wt15x10.d75r200j/Vp_model.dat

Recovered Vs Structure:

/ld4/OK_Gap/OK_Gap_NTS/Stevens_etal_2018_TomoDD/D15B_Synth_Runs/CX.y3x3zlp3n6p10n15_p3_Ov2z/I.wt15x10.d75r200j/Vs_model.dat

Post-Processed ASCII Tables Directory:

/ld4/OK_Gap/OK_Gap_NTS/Stevens_etal_2018_TomoDD/D15B_Synth_Runs/CX.y3x3zlp3n6p10n15_p3_Ov2z/I.wt15x10.d75r200j/output_files/

Best-Fit Inversion (Figures 1.11-1.15) – The initial best-fit inversion sub-directory location and input and output files. A copy of these files are included in the BestFitRun/ directory described at the top of this appendix.

Input Data Directory:

/ld4/OK_Gap/OK_Gap_NTS/Stevens_etal_2018_TomoDD/D15B_Param_Runs/0.1.Common_Inputs/

Station Locations:

/ld4/OK_Gap/OK_Gap_NTS/Stevens_etal_2018_TomoDD/D15B_Param_Runs/0.1.Common_Inputs/station.sel.dat

Initial Earthquake Sub-Catalog Locations:

/ld4/OK_Gap/OK_Gap_NTS/Stevens_etal_2018_TomoDD/D15B_Param_Runs/0.1.Common_Inputs/event.eq.sel

Phase Travel Time Data:

/ld4/OK_Gap/OK_Gap_NTS/Stevens_etal_2018_TomoDD/D15B_Param_Runs/0.1.Common_Inputs/absolute.dat

Differential Travel Time Data:

/ld4/OK_Gap/OK_Gap_NTS/Stevens_etal_2018_TomoDD/D15B_Param_Runs/0.1.Common_Inputs/dt.ct

Inversion Directory:

/ld4/OK_Gap/OK_Gap_NTS/Stevens_etal_2018_TomoDD/D15B_Param_Runs/wt15x10.d75r200j.tdd10rcmp

Recovered Vp Structure:

/ld4/OK_Gap/OK_Gap_NTS/Stevens_etal_2018_TomoDD/D15B_Param_Runs/wt15x10.d75r200j.tdd10rcmp/Vp_model.dat

Recovered Vs Structure:

/ld4/OK_Gap/OK_Gap_NTS/Stevens_etal_2018_TomoDD/D15B_Param_Runs/wt15x10.d75r200j.tdd10rcmp/Vs_model.dat

Relocated Earthquake Sub-Catalog:

/ld4/OK_Gap/OK_Gap_NTS/Stevens_etal_2018_TomoDD/D15B_Param_Runs/wt15x10.d75r200j.tdd10rcmp/test.reloc

Post-Processed ASCII Tables Directory:

/ld4/OK_Gap/OK_Gap_NTS/Stevens_etal_2018_TomoDD/D15B_Param_Runs/wt15x10.d75r200j.tdd10rcmp/output_files_3/

Increased Initial Velocity Model (Figures 2.4.A & 2.4.D) This inversion used the same input data and parameterization as the best-fit model, but used an altered input velocity structure (MOD) file with velocities 5% faster than those used in the best-fit model.

Input Data Directory:

/ld4/OK_Gap/OK_Gap_NTS/Stevens_etal_2018_TomoDD/D15B_Param_Runs/0.1.Common_Inputs/

Inversion Directory:

/ld4/OK_Gap/OK_Gap_NTS/Stevens_etal_2018_TomoDD/D15B_Param_Runs/wt15x10.d75r200j.D15_UP5/

Recovered Vp Structure:

/ld4/OK_Gap/OK_Gap_NTS/Stevens_etal_2018_TomoDD/D15B_Param_Runs/wt15x10.d75r200j.D15_UP5/Vp_model.dat

Recovered Vs Structure:

/ld4/OK_Gap/OK_Gap_NTS/Stevens_etal_2018_TomoDD/D15B_Param_Runs/wt15x10.d75r200j.D15_UP5/Vs_model.dat

Post-Processed ASCII Table:

/ld4/OK_Gap/OK_Gap_NTS/Stevens_etal_2018_TomoDD/D15B_Param_Runs/wt15x10.d75r200j.D15_UP5/test_Z6.00km.dat

Decreased Initial Velocity Model (Figures 2.4.B & 2.4.E). This inversion used the same input data and parameterization as the best-fit model, but used an altered input velocity structure (MOD) file with velocities 5% slower than those used in the best-fit model.

Input Data Directory:

/ld4/OK_Gap/OK_Gap_NTS/Stevens_etal_2018_TomoDD/D15B_Param_Runs/0.1.Common_Inputs/

Inversion Directory:

/ld4/OK_Gap/OK_Gap_NTS/Stevens_etal_2018_TomoDD/D15B_Param_Runs/wt15x10.d75r200j.D15_DN5/

Recovered Vp Structure:

/ld4/OK_Gap/OK_Gap_NTS/Stevens_etal_2018_TomoDD/D15B_Param_Runs/wt15x10.d75r200j.D15_DN5/Vp_model.dat

Recovered Vs Structure:

/ld4/OK_Gap/OK_Gap_NTS/Stevens_etal_2018_TomoDD/D15B_Param_Runs/wt15x10.d75r200j.D15_DN5/Vs_model.dat

Post-Processed ASCII Table (Figure 2.4.B & 2.4.E):

/ld4/OK_Gap/OK_Gap_NTS/Stevens_etal_2018_TomoDD/D15B_Param_Runs/wt15x10.d75r200j.D15_DN5/test_Z6.00km.dat

8629 Event sub-catalog and inversion (Figures 2.4.C & 2.4.F) This inversion used a sub-catalog that was declustered with smaller oblate spheroid, resulting in an increase earthquake density. Inversion parameterization was identical to the best-fit model.

Input Data Directory:

/ld4/OK_Gap/OK_Gap_NTS/Stevens_etal_2018_TomoDD/TomoDD_D15dense_Runs/0.1.Common_Inputs/

Inversion Directory:

/ld4/OK_Gap/OK_Gap_NTS/Stevens_etal_2018_TomoDD/TomoDD_D15dense_Runs/wt15x10.d200r200j/

Recovered Vp Structure:

/ld4/OK_Gap/OK_Gap_NTS/Stevens_etal_2018_TomoDD/TomoDD_D15dense_Runs/wt15x10.d200r200j/Vp_model.dat

Recovered Vs Structure:

/ld4/OK_Gap/OK_Gap_NTS/Stevens_etal_2018_TomoDD/TomoDD_D15dense_Runs/wt15x10.d200r200j/Vs_model.dat

Post-Processed ASCII Table:

/ld4/OK_Gap/OK_Gap_NTS/Stevens_etal_2018_TomoDD/TomoDD_D15dense_Runs/wt15x10.d200r200j/output_files_1/test_Z6.00km.dat

Reduced Spatial Scale Checkerboard Recovery Test - 2 node by 2 node experiment (Figures 2.5 – 2.8). This checkerboard recovery test had the same vertical distribution and polarity of imposed checkerboard anomalies as the 3 node by 3 node experiment (Figure 1.6), but used 2 node by 2 node anomalies for each checkerboard layer. Stages of this test match those described for the 3 node by 3 node data.

Forward Model Directory:

/ld4/OK_Gap/OK_Gap_NTS/Stevens_etal_2018_TomoDD/D15B_Synth_Runs/CX.y2x2zlp3n6p10n15_p3_Ov2z/F.Forward/

Synthetic Data Directory:

/ld4/OK_Gap/OK_Gap_NTS/Stevens_etal_2018_TomoDD/D15B_Synth_Runs/CX.y2x2zlp3n6p10n15_p3_Ov2z/T.Transfer/

Inverse Model Directory:

/ld4/OK_Gap/OK_Gap_NTS/Stevens_etal_2018_TomoDD/D15B_Synth_Runs/CX.y2x2zlp3n6p10n15_p3_Ov2z/I.wt15x10.d75r200j/

Recovered Vp Structure:

/ld4/OK_Gap/OK_Gap_NTS/Stevens_etal_2018_TomoDD/D15B_Synth_Runs/CX.y2x2zlp3n6p10n15_p3_Ov2z/I.wt15x10.d75r200j/Vp_model.dat

Recovered Vs Structure:

/ld4/OK_Gap/OK_Gap_NTS/Stevens_etal_2018_TomoDD/D15B_Synth_Runs/CX.y2x2zlp3n6p10n15_p3_Ov2z/I.wt15x10.d75r200j/Vs_model.dat

Post-Processed ASCII Tables Directory:

/ld4/OK_Gap/OK_Gap_NTS/Stevens_etal_2018_TomoDD/D15B_Synth_Runs/CX.y2x2zlp3n6p10n15_p3_Ov2z/I.wt15x10.d75r200j/output_files/